Banner appropriate to article type will appear here in typeset article

# Vorticity cascade and turbulent drag in wall-bounded flows: plane Poiseuille flow

Samvit Kumar<sup>1</sup>†, Charles Meneveau<sup>1</sup> and Gregory Eyink<sup>1,2</sup>

(Received xx; revised xx; accepted xx)

Drag for wall-bounded flows is directly related to flux of spanwise vorticity outward from the wall. In turbulent flows a key contribution arises from wall normal vorticity flux by nonlinear advection and stretching of vorticity, which can also be interpreted as a cascade. We study this process using numerical simulation data of turbulent channel flow at  $Re_{\tau} = 1000$ . The net transfer from the wall of fresh spanwise vorticity created by downstream pressure drop is due to two large opposing fluxes, one which is "down-gradient" or outward from the wall, where most vorticity concentrates, and the other which is "up-gradient" or toward the wall and acting against strong viscous diffusion in the near-wall region. We present evidence that the up-gradient transport occurs by a mechanism of correlated inflow and spanwise vortex stretching that was proposed by Lighthill. This mechanism is essentially Lagrangian, but we explicate its relation to the Eulerian anti-symmetric vorticity flux tensor. As evidence for the mechanism we study (i) statistical correlations of the wall-normal velocity and of wall-normal flux of spanwise vorticity, (ii) vorticity flux cospectra that identify eddies involved in nonlinear vorticity transport in the two opposing directions, and (iii) visualizations of coherent vortex structures which contribute dominantly to the transport. The "D-type" vortices contributing dominantly to down-gradient transport in the log-layer are found to be attached, hairpin-type vortices. However, the "U-type" vortices contributing dominantly to up-gradient transport are detached, wall-parallel, pancake-shaped vortices with strong spanwise vorticity, as expected by Lighthill's mechanism. We discuss modifications to the attached eddy model and implications for turbulent drag reduction.

## 1. Introduction

Most current approaches to wall-bounded turbulence are based on momentum conservation and the concept of "momentum cascade" to the wall (Tennekes & Lumley 1972; Jiménez 2012; Yang *et al.* 2016). However, vorticity conservation may arguably be of equal or even greater importance. One of the earliest advocates of this point of view was Taylor (1932), although his "vorticity transfer hypothesis" was justly criticized for neglect of vortex-stretching. Nevertheless, Taylor arrived at an important exact result that pressure drop in turbulent flow down a pipe is directly related to flux of spanwise vorticity across the flow. Lighthill (1963) was an even more forceful champion for vorticity-based approaches, positing that "to explain convincingly the existence of boundary layers ...arguments concerning

† Email address for correspondence: skumar67@jh.edu

<sup>&</sup>lt;sup>1</sup>Department of Mechanical Engineering, The Johns Hopkins University, Baltimore, Maryland, USA

<sup>&</sup>lt;sup>2</sup>Department of Applied Mathematics, The Johns Hopkins University, Baltimore, Maryland, USA

vorticity are needed" and further that "vorticity considerations ... illuminate the detailed development of the boundary layers just as clearly as do momentum considerations." In particular, Lighthill (1963) argued that vorticity is uniquely suited to a causal description of fluid flows, as it is the only variable whose effects propagate at finite speeds in the incompressible limit.

Lighthill made in fact substantial concrete contributions to the program of explaining turbulent boundary layers by means of vorticity dynamics. One key idea introduced by Lighthill (1963) which is now widely recognized is that vorticity generation at solid walls is due to tangential pressure gradients, with wall-normal vorticity flux given by

$$\boldsymbol{\sigma} = \mathbf{n} \times (\nu \nabla \times \boldsymbol{\omega}) = -\mathbf{n} \times (\nabla p + \partial_t \mathbf{u}), \tag{1.1}$$

where  $\bf n$  is the unit normal vector at the boundary pointing inward to the fluid. The term  $\partial_t {\bf u}$  which accounts for tangential acceleration of the wall was introduced by Morton (1984), who emphasized further the inviscid character of such vorticity production. Although generally well accepted, the relations (1.1) have been the subject of some minor controversy, since they were first derived by Lighthill (1963) only for flat walls and were generalized subsequently to curved walls in the form (1.1) by Lyman (1990) and in an alternative form  $\sigma' = -v(n \cdot \nabla)\omega$  by Panton (1984). The subsequent debate over which of these two forms is "correct" is reviewed by Terrington *et al.* (2021), who conclude that the two expressions measure slightly different things and have each their own (overlapping) domains of applicability. See also Wang *et al.* (2022). Lyman's version (1.1) uniquely describes the creation of circulation at the boundary (Eyink 2008) and we use that form in our theoretical discussion here (but note the two coincide in our concrete application to channel flow). In either guise, the Lighthill source reveals that the solid walls are the ultimate origin of all vorticity in the flow, whereas for momentum the walls act instead as the sink. In consequence, the profound sensitivity of fluid flows to the nature of the solid boundary is better revealed by vorticity considerations.

Lighthill (1963) made another essential contribution to wall-bounded turbulence which seems, however, to have been less appreciated. To introduce Lighthill's basic insight, we can do no better than to quote at length from his own paper:

"The main effect of a solid surface on turbulent vorticity close to it is to correlate inflow towards the surface with lateral stretching. Note that only the stretching of vortex lines can explain how during transition the mean wall vorticity increases as illustrated in Fig.II.21; and only a tendency, for vortex lines to stretch as they approach the surface and relax as they move away from it, can explain how the gradient of mean vorticity illustrated in Fig.II.21 is maintained in spite of viscous diffusion down it — to say nothing of any possible 'turbulent diffusion' down it, which the old 'vorticity transfer' theory supposed should occur. It is relevant to both these points that Fig.II.21 relates to uniform external flow, which implies zero mean rate of production of vorticity at the surface; but, even in an accelerating flow, the rate of production UU' is too small to explain either.

A simplified illustration of how inflow towards a wall tends to go with lateral stretching, and how outflow with lateral compression, is given in Fig.II.22. Doubtless some longitudinal deformation is usually also present, which reduces the need for lateral deformation (perhaps, on average, by half). However, there is evidence (from attempts to relate different types of theoretical model of a turbulent boundary layer to observations by hotwire techniques; see, for example, Townsend 1956) that the larger-scale motions (which push out 'tongues' of rotational fluid discussed above) are elongated in the stream direction, as if their vortex lines had been stretched longitudinally by the mean shear; in such motions, the correlation between inflow and lateral stretching illustrated in Fig.II.22 would be particularly strong. We may think of them as constantly bringing the major part of the vorticity in the layer close to the wall, while intensifying it by stretching and, doubtless, generating new

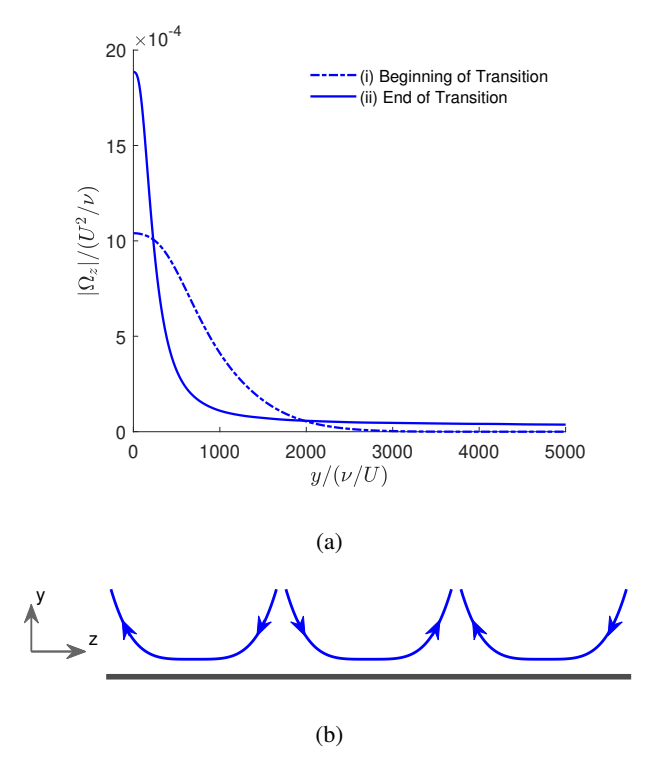


Figure 1: Close facsimiles of figures from Lighthill (1963). (a) An adaptation of Fig.II.21, with the original caption reading: "Distribution of mean vorticity in a boundary layer with uniform external flow; (i) at the beginning, (ii) at end, of transition", using data from JHTDB ( Li *et al.* (2008); Zaki (2013)). (b) An adaptation of Fig.II.22, original caption reading: "Correlation of inflow with lateral stretching, and outflow with lateral compression, of vortex lines (the mean flow is normal to the plane of the paper)".

vorticity at the surface; meanwhile, they relax the vortex lines which they permit to wander into the outer layer. Smaller-scale movements take over from these to bring vorticity still closer to the wall, and so on. Thus, the 'cascade process', which in free turbulence (see, for example, Batchelor 1953) continually passes the energy of fluctuations down to modes of shorter and shorter length-scale — because at high Reynolds numbers motions in a whole range of scales may be unstable, which implies that motions of smaller scale can extract energy from them—this cascade process has the additional effect in a turbulent boundary layer of bringing the fluctuations into closer and closer contact with the wall, while their vortex lines are more and more stretched." —From Lighthill (1963), pp.98-99.

We find in this remarkable passage four key ideas: (i) First, the correlation between turbulent inflow and lateral vortex stretching illustrated by Lighthill (1963) with his Figure II.22 acts to magnify principally spanwise vorticity and to drive it nearer the wall as shown in his Figure II.21 (both reproduced here as our Figure 1). Quoting again from Lighthill (1963), p.96, "it concentrates most of the vorticity much closer to the wall than before, although at the same time allowing some straggling vorticity to wander away from it farther." The validity of this mechanism for a transitional boundary-layer flow has been verified recently by Wang *et al.* (2022). One would expect on the basis of this argument to find spanwise-extended vortex structures as principal elements of wall-bounded turbulent flows. Conversely, turbulent upflow is correlated with lateral vortex compression, weakening the mainly spanwise vorticity as

it is driven away from the wall. (ii) The mechanism of correlated inflow and vortex-stretching is powerfully up-gradient, acting against both viscosity and "eddy-viscosity" effects which attempt to smooth the very sharp gradients of vorticity created near the wall. As remarked by Lighthill (1963),p.96, "turbulence redistributes the vorticity in such a way that viscous diffusion becomes more effective in countering the amplitude of the disturbances." (iii) This intense competition between up-gradient vortex-stretching on the one hand and diffusion away from the wall by molecular and turbulence effects on the other is narrowly won by the latter, since the net vorticity produced at the wall by the Lighthill source (1.1) must be transferred away under statistically steady conditions. Note that Lighthill's argument presumes that the total pressure  $p + (1/2)|\mathbf{u}|^2$  is continuous across accelerating turbulent boundary layers, so that the mean vortex production at the wall with steady, external mean velocity  $U = \langle u \rangle$  is given by  $U \partial_x U$ . (iv) Finally, Lighthill saw this up-gradient transport of vorticity toward the wall as a scale-by-scale cascade process, proceeding by the successive stretching, straightening, and strengthening of spanwise vorticity through a hierarchy of eddy scales. Among the chief results of the present work will be direct empirical confirmation of these insights of Lighthill.

Closely related ideas were developed somewhat after Lighthill's work in the adjacent field of quantum superfluids, where Josephson (1965) for superconductors and Anderson (1966) for neutral superfluids recognized the relation between drops of voltage/pressure in flow through wires/channels and the cross-stream flux of quantized magnetic-flux/vortex lines. Their ideas closely mirror those of Taylor (1932) and Lighthill (1963) for classical fluids, but Josephson (1965) and Anderson (1966) were seemingly unaware of those earlier works and the two literatures have subsequently developed in parallel. In quantum superfluids the Josephson-Anderson relation has become the paradigm to explain drag and dissipation in otherwise ideal superflow (Packard 1998; Varoquaux 2015). This understanding is based in particular on the work of Huggins (1970), who derived a "detailed Josephson-Anderson relation" that exactly relates energy dissipation to vortex motions. Interestingly, although the target application of Huggins (1970) was quantum superfluids, his mathematical model was the incompressible Navier-Stokes equation for a classical viscous fluid. In fact, somewhat later Huggins (1994) applied his ideas to classical turbulent channel flow.

More precisely, Huggins (1970, 1994) considered a classical incompressible fluid at constant density  $\rho$  and with kinematic viscosity  $\nu$  flowing in a channel with accelerations due both to a conservative force  $-\nabla Q$  and to a non-conservative force  $-\mathbf{g}$  (with  $\nabla \times \mathbf{g} \neq \mathbf{0}$ ), described by

$$\partial_t \mathbf{u} = \mathbf{u} \times \boldsymbol{\omega} - \nu \nabla \times \boldsymbol{\omega} - \nabla (p/\rho + |\mathbf{u}|^2/2 + O) - \mathbf{g}. \tag{1.2}$$

For example, Q might be the gravitational potential energy density  $\rho gy$  for vertical height y (with acceleration due to gravity g), and  $\mathbf{g}$  might be  $-\nabla \cdot \boldsymbol{\tau}_p$  with  $\boldsymbol{\tau}_p$  the stress of a polymer additive. Huggins (1970, 1994) noted that this equation for the momentum balance may be rewritten as

$$\partial_t u_i = (1/2)\epsilon_{ijk} \Sigma_{jk} - \partial_i h, \tag{1.3}$$

with anti-symmetric vorticity flux tensor

$$\Sigma_{ij} = u_i \omega_j - u_j \omega_i + \nu \left( \frac{\partial \omega_i}{\partial x_i} - \frac{\partial \omega_j}{\partial x_i} \right) - \epsilon_{ijk} g_k, \tag{1.4}$$

and total pressure or enthalpy

$$h = p/\rho + |\mathbf{u}|^2/2 + Q. \tag{1.5}$$

Here the total pressure h includes both the hydrostatic and the dynamic pressures, and the

tensor  $\Sigma_{ij}$  represents the flux of the *j*th vorticity component in the *i*th coordinate direction. The latter interpretation is made clear by taking the curl of the momentum equation (1.2), which yields a local conservation law for vector vorticity:

$$\partial_t \omega_i + \partial_i \Sigma_{ij} = 0. \tag{1.6}$$

The first term in (1.4) for  $\Sigma_{ij}$  represents the advective transport of vorticity, the second represents transport by nonlinear stretching and tilting, the third represents viscous transport, and the fourth represents transport of vorticity perpendicular to an applied, non-conservative body-force  $\mathbf{g}$  akin to the Magnus effect. The stretching /tilting term in the Helmholtz equation is not ordinarily understood as representing a space transport of vorticity but it can be interpreted in that sense (see section 2). The equation (1.3) thus shows the deep connection between momentum balance and vorticity transport, and this equation is the most elementary version of the classical Josephson-Anderson relation. See also the more recent work of Terrington *et al.* (2021), who discuss at length the meaning and applications of the antisymmetric vorticity flux tensor (1.4), which they call the "Lyman-Huggins tensor".

A first attempt was made by Eyink (2008) to unify these parallel theories in the context of two canonical turbulent flows, plane-parallel channels and straight pipes. He discussed the physical significance of the observation by Taylor (1932) and by Huggins (1994) that there is a mean cross-stream vorticity flux driven by the downstream pressure gradient. In the context of channel flow, with x the streamwise direction, y the wall-normal direction, and z the spanwise direction, this average relation takes the form

$$\langle \Sigma_{yz} \rangle = \langle v\omega_z - w\omega_y - v(\partial_y \omega_z - \partial_z \omega_y) \rangle = \partial_x \langle p \rangle = -u_\tau^2 / h, \tag{1.7}$$

where  $\Sigma_{yz}$  is the wall-normal flux of spanwise vorticity, h is the channel half-height, and  $u_{\tau}$  is the friction velocity. The standard result that  $\partial_y \partial_x \langle p \rangle = 0$  (Tennekes & Lumley (1972), section 5.2) is seen to be a consequence of vorticity conservation  $\partial_y \langle \Sigma_{yz} \rangle = 0$ . Eyink (2008) noted that Huggins' vorticity flux tensor (1.4) and Lighthill's vorticity source (1.1) in the form of Lyman (1990) are simply related by  $\sigma = \mathbf{n} \cdot \mathbf{\Sigma}$ , so that the origin of the constant mean flux is the vorticity created at the wall, which flows toward the channel center to be annihilated by opposite-sign vorticity from the facing wall. Eyink (2008) referred to this phenomenon as an "inverse vorticity cascade", but note that the vorticity transport involved here is down-gradient, opposed by the up-gradient cascade mechanism proposed by Lighthill (1963). The term "inverse cascade" was used by Eyink (2008) because the vorticity flux is in the opposite direction as the flux of momentum, that is, out from the wall and via eddies of increasing size at further distances from the wall. Just like momentum flux in wall-bounded turbulence is also called a cascade (Tennekes & Lumley (1972); Jiménez (2012)) because it involves momentum transfer in space and scale, we follow Eyink (2008) and refer to vorticity flux as a cascade as well since it involves vorticity transfer in space and in scale.

A possible mechanism for this cascade (or flux) is lifting and growing hairpin-like vortex structures in the inertial sublayer of the channel flow. It was shown by Eyink (2008) that constant mean down-gradient flux of vorticity via the nonlinear dynamics can in fact be explained by the attached-eddy model (AEM) of Townsend (1976) (see Marusic & Monty (2019) for a recent comprehensive review). Since the AEM is not designed to describe the statistics and dynamics of the fine-grained vorticity (Marusic & Monty (2019), section 4.1), it is not entirely trivial that the model should account for the mean vorticity flux. However, this flux can be deduced from the Reynolds stress by the standard relation (Taylor 1915; Tennekes & Lumley 1972; Klewicki 1989)

$$\langle v\omega_z - w\omega_y \rangle = -\partial_y \langle u'v' \rangle, \tag{1.8}$$

from which it can be shown that the AEM implies  $\langle v\omega_z - w\omega_y \rangle \sim -u_\tau^2/h$  for  $y \gtrsim y_p$ , where

 $y_p$  is the wall distance of the peak Reynolds stress (Eyink 2008). On the contrary, for  $y < y_p$  it follows directly from (1.8) that  $\langle v\omega_z - w\omega_y \rangle > 0$ , whose positive sign indicates up-gradient nonlinear transport of (negative) spanwise vorticity. It was noted by Eyink (2008) that this up-gradient transport is not obviously explained by attached eddies and we shall present here strong evidence that the underlying mechanism is in fact that of Lighthill (1963). A further impetus to our investigation comes from recent work of Eyink (2021), who showed that the "detailed relation" of Huggins (1970) for energy dissipation in channel flows holds also for flow around a uniformly moving solid body. In fact, this result holds much more generally for bodies that are moving non-uniformly and even changing shape and volume (Eyink, unpublished) and also for channel flows with periodic boundary conditions (Kumar & Eyink 2023). In all of these situations, there is flux of vorticity away from the solid surface and net drag is given instantaneously by the spatial integral of spanwise vorticity flux across the streamlines of a background potential Euler flow.

The nonlinear flux of spanwise vorticity  $\langle v\omega_z - w\omega_y \rangle$ , also interpreted as a 'turbulent inertia (TI)' term, defined as the wall-normal gradient of Re shear stress  $(\partial_v \langle -u'v' \rangle)$ , has been studied in several previous works. Experimental measurements of  $\langle v\omega_z \rangle$  and  $\langle w\omega_y \rangle$ contributions were measured separately (Klewicki (1989)). In addition, weighted PDFs of fluctuations of v with  $v\omega_z$  and w with  $w\omega_v$  were calculated (Klewicki et al. (1994)). A fourlayer structure for wall-bounded flows was proposed by Wei et al. (2005), based on the relative magnitude of the viscous and TI term in the mean momentum equation (see also Klewicki et al. (2007)). The wall-normal derivative of streamwise spectra of the Reynolds' shear stress, equal to the nonlinear flux co-spectra for periodic flows, was studied as the 'Net Force Spectra' for pipe flows (Guala et al. (2006)), channel flows and zero pressure gradient boundary layers(Balakumar & Adrian (2007)). An in-depth study of the statistics and streamwise spectral behavior of the velocity-vorticity products for turbulent boundary layers, at several Re values, was carried out by Priyadarshana et al. (2007). They compared streamwise spectra for velocity and vorticity with the corresponding co-spectra and plotted profiles of the velocity-vorticity products and correlation coefficients. The correlations between velocity and vorticity are seen to arise from a 'scale selection' associated with peaks in the velocity and vorticity streamwise spectra. Monty et al. (2011) interpret the TI term as a momentum source/sink (depending upon the sign) and carried out detailed calculations of the streamwise and spanwise two-point correlations of v with  $\omega_z$  and w with  $\omega_y$ . They draw an important conclusion that anticipates our own, that "the mean Reynolds stress gradient at any wallnormal location is a direct result of a slight asymmetry in the characteristic vortical motions of the flow". Morrill-Winter & Klewicki (2013) carried out experimental investigations along similar lines for flat plate boundary layers. They study streamwise co-spectra, scale selection, two-point correlations, and Reynolds number effects, highlighting the fact that the mean effect of TI can be expressed as a difference between two velocity vorticity correlations, which can be related to change of scale effects  $(-w\omega_v)$  and to advective transport  $(v\omega_z)$ . Chin et al. (2014) continued work on this theme by conducting a detailed analysis of the TI term for pipe flows using direct numerical simulations. They decompose the TI term into advective transport and vorticity stretching and/or reorientation and carry out a detailed study of the wall-normal variation of the respective streamwise co-spectra and the combined 'Net force spectrum'. Calculations of joint probability density functions (p.d.fs) are done and apart from a focus on investigating the Reynolds number dependence of the Reynolds shear stress peak location. Brown et al. (2015) are also motivated by the work of Taylor (1915, 1932) which first drew attention to the connection between transport of vorticity and the Reynolds stress and study vorticity flux in channel flows using Direct Numerical Simulation data for channel flows over a range of Re. They highlight the fact that the total mean vorticity flux is constant across every wall parallel plane for a turbulent pressure-driven channel flow and study the two nonlinear contributions to the flux. Of particular interest, is their calculation of the p.d.fs of  $w\omega_{\rm v}$  close to the wall and their visualization of the vortex lines passing through such a region. The work of Wu et al. (2012), primarily studied streamwise very large-scale motions (VLSMs) and their relations to Re-stress in pipe flows. They made an important contribution to the study of vorticity flux by plotting for the first time (with brief discussions), 2-D 'Net force spectra' at four wall-normal locations, scaled with outer units. Since they were mainly focused on streamwise spectra, they did not plot these scaled with wall distance and were unaware of relations with Lightill's mechanism. However, we follow their work in calculating 2-D co-spectra here for channel flow and find that scaling with the wall-normal distance, instead of inner or outer units, provides important insights into the dynamics at play (see section 3.3 for further details). Experimental measurements for an open channel flow by Chen et al. (2014) focused on the contributions of spanwise vortex filaments to Reynolds shear stress and to  $v\omega_z$ . Apart from measuring separate contributions to the advection term from prograde and retrograde vortices, they observe that the movement away from the wall yields the significant contribution of spanwise vortex filaments (identified by a swirling strength-based criterion) to the 'net force'. These ideas are further explored in Chen et al. (2018b) where flow structures are classified into four groups based on vorticity and swirling strength. Contributions made by the structures to the nonlinear vorticity fluxes are measured, we follow a similar approach in the present study as well.

To gain further insight into the underlying fluid-dynamical mechanisms of turbulent vorticity flux, we here carry out a detailed investigation of the turbulent vorticity dynamics in the simplest case of turbulent channel flow. Although viscous diffusion plays a dominant role in the mean vorticity transport out to the wall distance  $y_p$  (Klewicki et al. 2007; Eyink 2008; Brown et al. 2015), its properties follow directly from the mean velocity profile and are thus relatively easy to understand. We shall therefore be more concerned with the nonlinear vorticity dynamics and the resulting statistics of the velocity-vorticity correlations  $\langle v\omega_z \rangle$ ,  $\langle w\omega_y\rangle$  at various wall distances. We employ data for our study from the Johns Hopkins Turbulence database (JHTDB) which stores the output of a direct numerical simulation of turbulent channel flow at  $Re_{\tau} = 1000$  (Li et al. 2008; Graham et al. 2016). This simulation was performed using the petascale DNS channel flow code PoongBack (Lee et al. 2013) with driving force provided by a constant applied pressure gradient. The resulting online database archives full space-time fields of velocity and pressure throughout the channel domain and for about one flow-through time. The archived data permit us to calculate not only the velocity-vorticity correlations but also their Fourier cospectra in streamwise wavenumber  $k_x$ , spanwise wavenumber  $k_z$  and 2D wavenumber  $(k_x, k_z)$ . We discuss related prior results by experiment, such as Klewicki (1989); Klewicki et al. (1994); Priyadarshana et al. (2007); Morrill-Winter & Klewicki (2013); Chen et al. (2014) and also by numerical simulation, including Bernard (1990); Crawford & Karniadakis (1997); Monty et al. (2011); Brown et al. (2015); Yoon et al. (2016); Chen et al. (2018b); Vidal et al. (2018).

We compute 2D cospectra for channel flow, which prove particularly illuminating of the physics. These cospectra, together with statistics conditioned on the sign of the wall-normal velocity in conjunction with vortex visualizations, yield evidence to support Lighthill's mechanism.

The detailed contents of this paper are outlined as follows. In section 2 we discuss how Lighthill's Lagrangian mechanism is represented by the Eulerian vorticity flux tensor, a necessary theoretical prelude so that our subsequent numerical results can be appropriately interpreted. The main section 3 of the paper presents our numerical study. In section 3.1 we study the mean vorticity flux and its component velocity-vorticity correlations, validating our own numerical results against previously published results and illustrating the mean flow of vorticity along isolines of total pressure. The next section 3.2 presents results on conditional

averages of fluxes given the direction of the wall-normal velocity as inward or outward, in order to investigate the proposed strong correlation. Section 3.3 presents results on cospectra of the nonlinear vorticity flux and velocity-vorticity correlations, both 1D spectra in the streamwise and spanwise wavenumbers and joint 2D spectra. Then in section 3.4 we use the 2D cospectra to divide the velocity and vorticity fields into "down-gradient" and "upgradient" eddy contributions and we visualize the coherent vortices which dominate transport in both of these components. Finally, in the conclusion section 4 we review our main results, draw relevant lessons and discuss important future directions. Incidental numerical results of various sorts are presented in Supplementary Materials.

# 2. Lighthill Mechanism and Huggins' Vorticity Flux Tensor

In order to properly interpret the results of our numerical study, we must first discuss carefully the physical and mathematical meaning of Lighthill's arguments. This is necessary especially because Lighthill's dynamical picture is essentially Lagrangian whereas Huggin's vorticity flux tensor (1.4) is Eulerian. Thus, the relation between Lighthill's mechanism and the predicted behaviour of Huggins' flux can be somewhat subtle and even counter-intuitive.

The basic picture behind Lighthill's argument is sketched as a cartoon in Fig. 2. Shown there is a representative vortex line carrying spanwise vorticity and also wall-normal vorticity associated to a lifted arch. If the flow is inward toward the wall (v < 0) at this location, then, by incompressibility, there must be diverging flow in the spanwise and/or streamwise directions. This divergent flow should generate corresponding velocity gradients in those directions which Lighthill argued should be strongest spanwise because the well-known longitudinal organization of the near-wall structures would tend to reduce streamwise gradients. According to the Helmholtz laws of ideal vortex dynamics, one would therefore expect the vortex line to be, first, carried down by the flow closer to the wall, and, second, flattened and stretched out, principally in the spanwise direction. This action of the Lagrangian flow is indicated by the blue dashed arrows in Fig. 2 which depict typical particle trajectories. Since the stretched vortex line should intensify, Lighthill suggested that the plausible result would be increased spanwise vorticity concentrated closer to the wall. The opposite effect should occur in regions of flow outward from the wall (v > 0), which corresponds to the same cartoon but reversing all velocity vectors given by red arrows and all Lagrangian trajectories given by blue dashed lines. In this case the vortex line according to ideal laws would be lifted away from the wall, compressed in the spanwise direction and correspondingly weakened. Such motions, according to Lighthill, would reduce the spanwise vorticity at further distances from the wall, so that the net effect of both types of motion would be an increase in the intensity of vorticity at the wall and a steepening of its wall-normal gradient. However, note that according to the Kolmogorov theory of local isotropy (Tennekes & Lumley (1972)), streamwise and spanwise velocity gradients may be of a similar magnitude at small enough scales. Therefore, the association of inflow with stretching of spanwise aligned vortex lines is expected to be primarily valid at scales that are large enough to possess the streamwise organization associated with stronger spanwise gradients. Similar scales should also be responsible for the down-gradient contribution associating outflow with the relaxation of spanwise vortex lines.

An obvious concern with this picture is its neglect of viscous diffusion effects, which certainly must be substantial in the near-wall buffer layer and viscous sublayer. In fact, as noted above, viscous diffusion dominates the average wall-normal flux of spanwise vorticity out to the location  $y_p$  of peak Reynolds stess (Klewicki *et al.* 2007; Eyink 2008; Brown *et al.* 2015). The viscous modifications of ideal vortex dynamics can be incorporated by means of a stochastic Lagrangian formulation of incompressible Navier-Stokes in vorticity-velocity

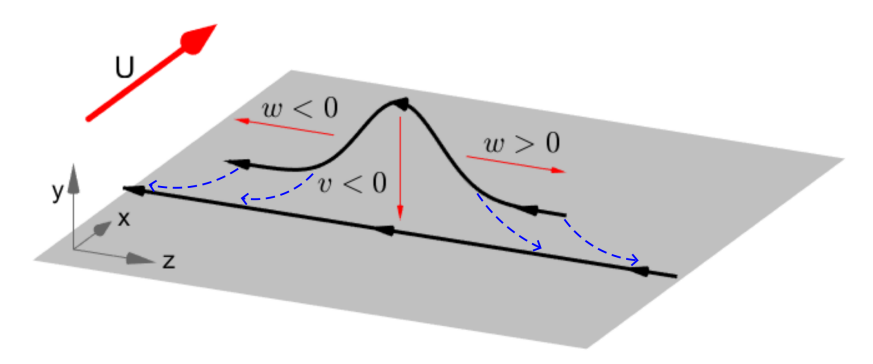


Figure 2: Cartoon of the "up-gradient" transport mechanism. For the "down-gradient" mechanism, the dashed blue arrows and the thin red arrows are reversed

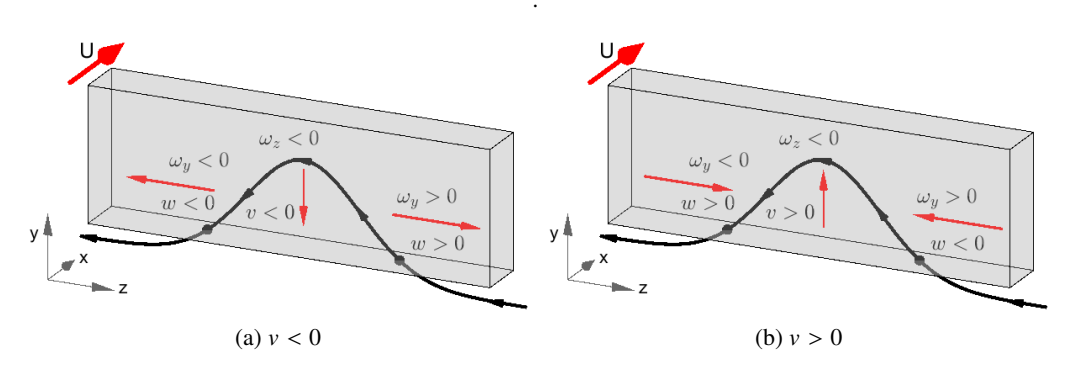


Figure 3: Control volume analysis of Lighthill's Mechanism ("vortex lines to stretch as they approach the surface and relax as they move away from it"), showing (a) inward flow (v < 0) and (b) outward flow (v > 0) from the wall, around a typical vortex line occupying a wall normal region corresponding to the buffer and log layers.

representation (Constantin & Iyer 2011; Eyink et al. 2020a), which represents viscous diffusion of vorticity by an average over stochastic Brownian perturbations of Lagrangian particle motions. This approach was exploited by Wang et al. (2022) to investigate the origin of the enhanced wall vorticity and skin friction in a transitional zero pressure-gradient boundary layer, as discussed in the passage from Lighthill (1963) quoted in the Introduction. This study used the Lighthill vorticity source  $\sigma$  in (1.1) as Neumann boundary conditions, so that the wall vorticity at points of local maximum amplitude could be expressed in terms of two contributions: (i) the Lighthill source integrated over earlier times and (ii) the initial conditions for the vorticity as modified by subsequent advection, stretching and viscous diffusion. It was found that the dominant source of the high wall-vorticity is the spanwise stretching of pre-existing spanwise vorticity, exactly as argued by Lighthill (1963). In particular, as also suggested by Lighthill, the rate of production by the vorticity source  $\sigma$ was "too small to explain" the maxima. This contribution was found in general to be about an order of magnitude smaller than that from spanwise stretching and also found to give vorticity contributions of both signs with about equal probability, thus often reducing the magnitude. The conclusion of Wang et al. (2022) from their analysis of the numerical data was that, despite strong viscous effects in the near-wall region, the theory of Lighthill (1963) explained well the origin of high wall-stress events observed in transitional flow.

The same stochastic Lagrangian methods can be applied also to fully-developed turbulent channel flow, but here, motivated by recent work of Eyink (2021); Kumar & Eyink (2023) on

the Josephson-Anderson relation, we instead aim to understand vorticity dynamics in terms of Huggins' vorticity current tensor (1.4). Because the vorticity conservation law (1.6) is expressed in Eulerian form, its relationship to Lighthill's Lagrangian picture is not entirely self-evident. The physical meaning of Huggins' tensor  $\Sigma_{ij}$  has previously been discussed by Terrington *et al.* (2021, 2022) using control volumes and control surfaces. To adapt their arguments, we integrate (1.6) over a volume V to obtain

$$\frac{d}{dt} \int_{V} \omega_{j} d^{3}x = -\oint_{\partial V} n_{i} \Sigma_{ij} dA \tag{2.1}$$

where n is the outward-pointing normal at the boundary  $\partial V$  and each individual term in  $n_i \Sigma_{ij}$ should represent a rate of change of  $\omega_I$  integrated over V. The meaning of the nonlinear term  $u_i \omega_i$  is transparent, as  $(\mathbf{n} \cdot \mathbf{u}) \omega_i$  just represents the advection of  $\omega_i$  across the boundary  $\partial V$ . The other nonlinear contribution  $-u_i\omega_i$  to the flux upon taking taking its divergence yields the term  $-(\omega \cdot \nabla)u$  in the Helmholtz equation associated to vortex stretching and tilting, so that it must somehow express that physics. It is worth remarking that Huggins (1994), p.326 concluded that this term "does not appear to have a particularly simple interpretation" but suspected that it is "a vortex stretching term". The relation with stretching/tilting is clarified by the Figure 3a which plots schematically the "up-gradient" configuration considered by Lighthill (1963) with flow inward to the wall advecting and stretching/tilting a hairpin-like vortex. We have drawn as control volume a rectangular box selected so that only the term  $-w\omega_{\rm v}$  in the flux  $\Sigma_{\rm vz}$  contributes to growth of spanwise vorticity  $\omega_{\rm z}$  in the volume, whereas the advection term  $v\omega_z$  does not contribute. Because of the diverging flow, two contributions with signs  $\omega_{\rm v} > 0$ , w > 0 and  $\omega_{\rm v} < 0$ , w < 0 occur at the bottom face of the box and these correspond indeed to an increase of (negative) spanwise vorticity in the pictured control volume, due to the lengthening of the spanwise vortex line segment and the tilting of the wall-normal vortex line segments.

It is notable that the contribution  $-w\omega_y < 0$  at the bottom face in Figure 3a corresponds to an *outward* flux of spanwise vorticity into the control volume, with a sign which is formally "down-gradient" or away from the wall. By contrast, for this inward flow configuration with v < 0, the advection term has sign  $v\omega_z > 0$  which is "up-gradient".

If we consider instead the outward flow configuration with v>0 (Figure 3b), which compresses and weakens the spanwise vorticity, then the signs would both reverse to  $v\omega_z<0$  and  $-w\omega_y>0$  (because of converging flow), but would remain opposite. The advective term is now making a "down gradient" contribution and the stretching/tilting term is making an "up gradient" contribution. The anti-correlated sign of the two flux contributions for inward (v<0), Figure 3a) and outward (v>0), Figure 3b) flows will be important in interpreting our numerical results below. It should be clear that this anti-correlation of signs depends upon the geometry of the vortex line. For example, if the vortex line in Figure 3a were instead bent inward into a U-shape and entered the control volume from the top face, then the sign of the stretching/tilting term would have become  $-w\omega_y>0$ . This would represent inward "up-gradient" flux into the control volume, positively correlated with the advection term  $v\omega_z>0$ . Thus, the relative signs of these terms potentially contains some information about the typical geometry of vortex lines.

To determine whether the net vorticity flux from nonlinearity is "up-gradient" or "down-gradient", it is important consider the combined term  $u_i\omega_j - u_j\omega_i$ , which is anti-symmetric. As stressed by Terrington *et al.* (2021), the anti-symmetry  $\Sigma_{ji} = -\Sigma_{ij}$  expresses the fundamental property that vortex lines cannot end in the fluid so that flux of  $\omega_j$  in the *i*th direction is necessarily associated with an equal and opposite flux of  $\omega_i$  in the *j*th direction. This relation of flux anti-symmetry and non-termination of vortex lines is clearly illustrated in Figure 3a. In the flow sketched there, the depicted spanwise flux  $\Sigma_{zy}$  of  $\omega_y$ -vorticity

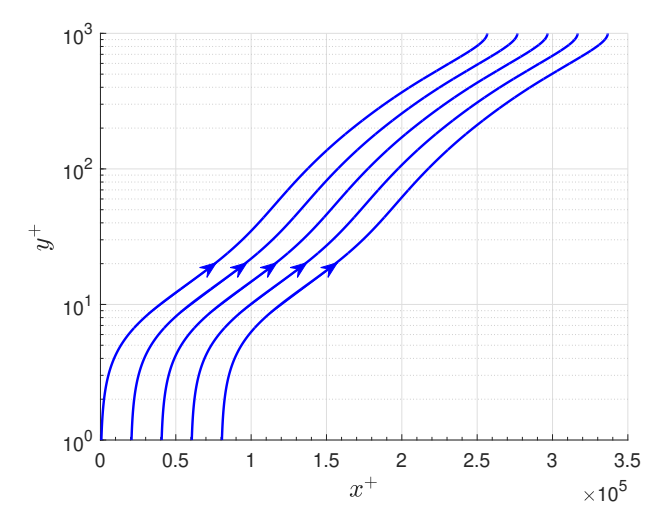


Figure 4: Flowlines of mean spanwise vorticity flux  $(\langle \Sigma_{xz} \rangle, \langle \Sigma_{yz} \rangle)$  obtained as the isolines of mean total pressure  $\langle h \rangle$ .

implies that the  $\omega_z$ -line must lengthen, because the vortex line which enters at one z-location in the bottom face must exit at the other. The resulting growth of  $\omega_z$ -vorticity in the interior corresponds to a wall-normal flux  $\Sigma_{yz} = -\Sigma_{zy}$  outward into the control volume. To determine from our numerical data whether nonlinear flux of spanwise vorticity is "down-gradient" or "up-gradient" it will therefore be crucial to consider the combined quantity  $v\omega_z - w\omega_y$  that contains both advection and stretching/tilting, since these two effects cannot be separated physically without violating the kinematic condition of non-terminating vortex lines.

## 3. Numerical Study of Vorticity Flux in Pressure-Driven Channel Flow

We now report on our empirical study of the flux of spanwise vorticity, hereafter referred to simply as "vorticity flux". This component of the vorticity is crucial to drag and energy dissipation, since its flux is directly related to streamwise pressure drop. As already mentioned in the Introduction (Sec 1), we employ direct numerical simulation data of channel flow at  $Re_{\tau} = 1000$  from the Johns Hopkins Turbulence Database (JHTDB) (see Li et al. (2008); Graham et al. (2016)). The right-handed Cartesian coordinate system for this data is the same as shown in Figures 2 & 3a, with x streamwise, y wall-normal and z spanwise. Although the database provides built-in tools to calculate velocity and vorticity gradients from Lagrange interpolants, our study of vorticity dynamics required greater accuracy for these crucial quantities. We have thus used the database cut-out service to download time snapshots of data for the entire channel. Gradients in the spanwise and streamwise directions are then calculated spectrally by FFT, and wall-normal gradients are calculated using seventh-order basis-splines based on the collocation points of the original simulation (Graham et al. (2016)). All statistics are thereafter calculated by averaging over wall-parallel planes in the x- and z-directions of homogeneity, as well as over multiple snaphots. The steady-state statistics presented here were calculated with 38 time snaphots. We shall generally plot our results only for the bottom half of the channel, with reflected results from the top half included to double the sample-size of our averages.

# 3.1. Mean vorticity flux and flow-lines

To provide an intuitive understanding of Huggins' vorticity flux tensor (1.4) and of the mean vorticity dynamics in turbulent channel flow, we first present numerical results on the average flux  $\langle \Sigma_{ij} \rangle$ . An important theoretical result which follows directly by averaging the momentum balance equation (1.3) is the steady-state relation between vorticity flux and the gradients of the total pressure:

$$\langle \Sigma_{ij} \rangle = \epsilon_{ijk} \partial_k \langle h \rangle. \tag{3.1}$$

This general result implies immediately for channel flow that

$$\langle \Sigma_{yz} \rangle = \partial_x \langle h \rangle, \quad \langle \Sigma_{xz} \rangle = -\partial_y \langle h \rangle, \quad \langle \Sigma_{xy} \rangle = 0,$$
 (3.2)

with all other components given by anti-symmetry. Since it is the flux of spanwise vorticity only which enters into the Josephson-Anderson relation for plane-parallel channel flow (Kumar & Eyink 2023) we shall focus on its dynamics in the (x, y)-plane (since  $\Sigma_{zz} = 0$ ). It can be very instructive about the physics to trace the integral flow lines of mean fluxes for transported quantities such as energy and momentum (Meyers & Meneveau 2013) and we carry out this construction for the conserved spanwise vorticity. Here there is a substantial simplification because, as a simple consequence of (3.2), the integral lines of the mean flux vector  $(\langle \Sigma_{xz} \rangle, \langle \Sigma_{yz} \rangle)$  coincide with the isolines of mean total pressure  $\langle h \rangle = P + \frac{1}{2}U^2 + \frac{1}{2}U^2$  $\frac{1}{2}\langle |u'|^2 + |v'|^2 + |w'|^2 \rangle$ . We follow the usual notations,  $U = \langle u \rangle$ , u' = u - U,  $P = \langle p \rangle$ , etc. In Figure 4 we plots these isolines resulting from numerical computation of  $\langle h \rangle$ . Consistent with the remark of Lighthill (1963) that "tangential vorticity created is in the direction of the surface isobars," the mean vorticity generated at the wall is spanwise and flows outward from points of constant  $\langle h \rangle = P$  at y = 0. The vorticity flux is about three orders of magnitude larger streamwise than wall normal, mainly because of the large term  $U\Omega_{\tau}$ contributing to  $\langle \Sigma_{xz} \rangle$ , with  $\Omega_z = -\partial_y U$ . Thus, the mean vorticity flow lines extend about 250 channel half-widths downstream as they cross from the wall to the channel center, reflecting the strong streamwise advection of vorticity. It is, however, the much smaller wall normal vorticity flux which is directly related to drag and energy dissipation, since  $\langle \Sigma_{vz} \rangle = \partial_x P$ by (3.2). As earlier remarked by Eyink (2008), the latter takes on the y-independent value  $\langle \Sigma_{yz} \rangle = -u_{\tau}^2/H$  because of the conservation relation  $\partial_y \langle \Sigma_{yz} \rangle = \partial_y \langle \Sigma_{yz} \rangle + \partial_x \langle \Sigma_{xz} \rangle = 0$  and the Lighthill (1963) relation for wall-generation of vorticity by tangential pressure gradients. This argument assumes as well the x-independence of steady-state averages such as  $\langle \Sigma_{xz} \rangle$ , which is evident in the parallel vorticity flux lines of Figure 4.

Exact results of Klewicki *et al.* (2007); Eyink (2008); Brown *et al.* (2015) for the nonlinear  $(v\omega_z - w\omega_y)$  and viscous  $(-v[\partial_y\omega_z - \partial_z\omega_y])$  contributions to the mean vorticity flux  $\langle \Sigma_{yz} \rangle$  provide a further check of the reliability of our numerics. Our numerical data are plotted in Fig 5 and show good agreement with the theoretically required behavior. First, we observe that the magnitude of the mean vorticity flux is constant in y to a very good approximation, except for small numerical oscillations very close to the wall  $(y^+ < 10)$ , and it matches quite well the average streamwise pressure gradient. This means that, on average, negative spanwise vorticity (the same sign as the mean vorticity) is being transported away from the wall and that overall, the flux is down-gradient. As in the Introduction, we shall refer to flux of vorticity away from the wall as "down-gradient," since the vorticity is already highly concentrated at the wall (Lighthill 1963), and flux in the opposite direction will be referred to as "upgradient". It was also shown by Klewicki *et al.* (2007); Eyink (2008); Brown *et al.* (2015) that, while viscous flux should be expected to be always down-gradient, the net nonlinear flux will be down-gradient above the height of the peak Reynolds' stress  $(y^+ = y_p^+ = 53)$  for the data at  $Re_\tau = 1000$  but up-gradient below that height and opposing the large viscous flux there. These theoretical results are well confirmed by our empirical data in Fig 5. In addition,

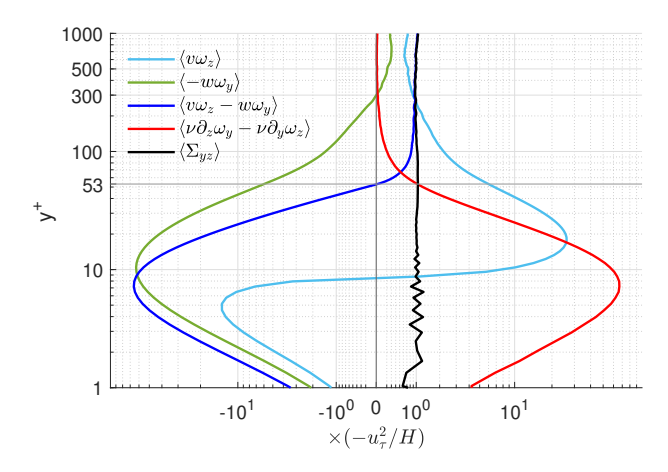


Figure 5: Vorticity flux in a pressure driven periodic channel, averaged in time as well as in the streamwise and spanwise directions. A good agreement is found with expected constant behaviour across the height of the channel. For  $y^+ < y_p^+ (= 53)$ , the nonlinear term gives a strong up-gradient contribution to the flux which is balanced by a larger down-gradient viscous contribution. As y increases above  $y_p$ , the nonlinear term contributes an increasing share of the down-gradient flux while the viscous contribution decreases as y grows, so that for  $y^+ \gtrsim 250$ , the nonlinear contribution carries nearly the entire vorticity flux.

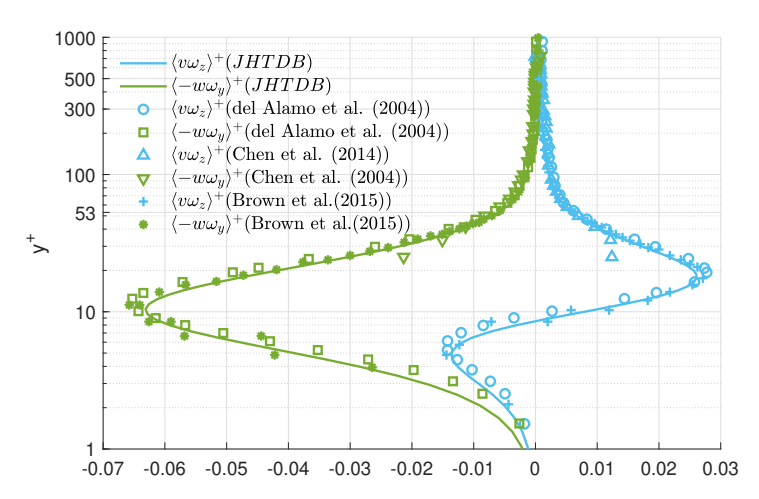


Figure 6: Contributions to nonlinear vorticity flux averaged over time and wall parallel planes, computed from channel flow data at  $Re_{\tau}=1000$  from JHTDB( Graham *et al.* (2016)) and from the earlier numerical simulation of channel flow at  $Re_{\tau}=1000$  by Brown *et al.* (2015),  $Re_{\tau}=934$  by Del Alamo *et al.* (2004), as reported in Monty *et al.* (2011), and from experimental measurements for an open channel flume at  $Re_{\tau}=740$  by Chen *et al.* (2014).

we have calculated the separate contributions of the advective  $(v\omega_z)$  and stretching/tilting  $(-w\omega_y)$  terms to the nonlinear flux, for which no exact predictions exist. However, our results for these two quantities plotted also in Fig. 6 agree well with those earlier reported by Monty et al. (2011); Brown et al. (2015); Chen et al. (2018b) from the channel-flow simulation of Del Alamo et al. (2004) at  $Re_\tau = 934$  and also with the experimental results of Chen et al. (2014) for an open channel flume at somewhat lower  $Re_\tau = 740$ . Similar observations have been made both at lower and at higher Reynolds numbers, but we postpone until our

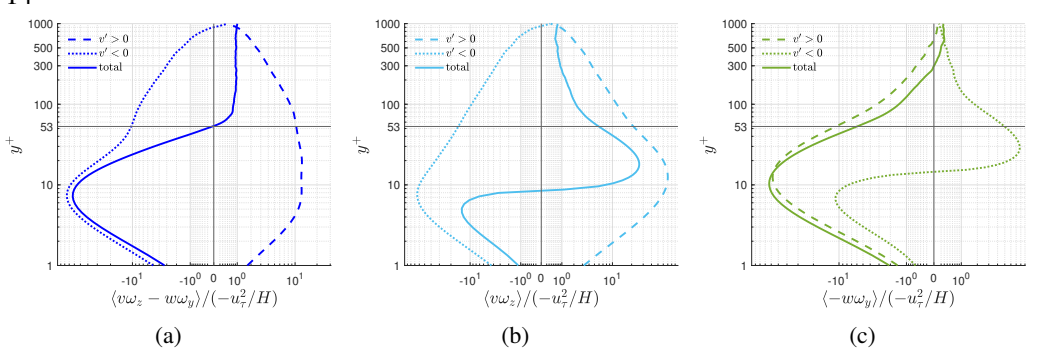


Figure 7: Contributions from regions where turbulent flow is outward  $(\nu' > 0)$  and inward  $(\nu' < 0)$ , to the (a) nonlinear flux, (b) convection/advection and (c) stretching/tilting, averaged over time and wall parallel planes, plotted as a function of wall distance.

conclusions section the discussion of the important issue of Re-dependences. Confirming those earlier studies, we find that both contributions are down-gradient in the outer range  $(y^+ \gtrsim 300)$  and both up-gradient in the near-wall  $(y^+ \lesssim 10)$ , but have opposite signs in the intermediate range corresponding roughly to the logarithmic mean velocity profile  $(30 \lesssim y^+ \lesssim 300)$ . Note that we use the term "log layer" for this range rather than the frequent term "inertial sublayer" because, as pointed out by Klewicki *et al.* (2007); Eyink (2008); Brown *et al.* (2015), viscous diffusion dominates mean vorticity transport at least up to  $y_p$ . In this logarithmic layer the nonlinear advection term is also down-gradient but the stretching/tilting term up-gradient, with advection dominating for  $y \gtrsim y_p$  and stretching/tilting dominating for  $y \lesssim y_p$ . The importance of the stretching/tilting term in the range  $y \lesssim y_p$  is suggestive of Lighthill's mechanism and the anti-correlation there is reminiscent of the opposite signs found in the control volume analysis of Figure 3. However, to identify precisely whether the vorticity up-gradient transport occurs by Lighthill's mechanism, we must study the crucial question of correlation with motion inward (v < 0) or outward (v > 0) from the wall.

# 3.2. Evidence for Lighthill's mechanism from flux-velocity correlations

A crucial feature of the theory of Lighthill (1963) is the proposed correlation between vorticity-strengthening and inward motion toward the wall, and likewise vorticity-weakening and outward motion away from the wall. To test for this key correlation we consider partial averages depending upon the two conditions v'>0 and v'<0, where the wall-normal velocity fluctuation is v'=v since V=0. Note that by "partial average subject to X" we mean the average conditioned upon the event X but further multiplied by the probability of X. Defined in this manner, the sum of the partial averages for the two exclusive events v'>0 and v'<0 yields the total average. In Fig. 7a we plot these partial averages for the total nonlinear flux  $v\omega_z-w\omega_y$ . Although Lighthill's proposed mechanism is essentially Lagrangian, we see a clear correlation in the Eulerian vorticity flux, with outflow (v>0) associated at all wall distances to down-gradient mean vorticity flux and inflow (v<0) associated to up-gradient mean flux, except possibly very near the center of the channel. The inflow contribution appears to prevail for  $y< y_p$ , where the net nonlinear flux is up-gradient. To gain further insight into the vorticity dynamics, we consider next the partial averages of the separate flux contributions from advection and stretching/tilting.

The partial averages of advective vorticity flux  $v\omega_z$  are plotted in Fig. 7b, which exhibit the same correlation as the total: down-gradient flux is associated to outflow and up-gradient flux to inflow (except at the channel center). This correlation is essentially obvious in the near-wall region since instantaneous vorticity has the sign  $\omega_z < 0$  nearly always there, the

same sign as the mean vorticity  $\Omega_z < 0$ . Note that the partial average from outflow prevails above the buffer layer, where the combined average is down-gradient. The dominance of outflow over inflow can be easily understood if the wall-normal velocity magnitudes |v| are roughly comparable for the two events, but if spanwise vorticity magnitudes  $|\omega_z|$  are generally greater for flows originating near the wall. We can thus have net advection of vorticity away from the wall, even though there is no net advection of mass. In contrast to this down-gradient behaviour in the log layer, we note that net mean advection is up-gradient for  $y^+ < 10$ . This result is plausibly explained if inflow events are correlated with locally higher spanwise vorticity due to stretching of spanwise aligned vortex lines in the near-wall region and outflow events with locally weaker vorticity due to relaxation and attenuation of vortex lines.

These conclusions and interpretations agree with earlier work of Klewicki *et al.* (1994), who measured experimentally the joint PDF  $P(v', \omega_z')$  of the fluctuations of wall-normal velocity v' and spanwise vorticity  $\omega_z'$  in a turbulent zero pressure-gradient boundary-layer. Their results showed for  $y^+ = 5.3$  that the mean  $\langle v'\omega_z' \rangle$  gets most of its contribution from quadrants Q1 and Q4 where v' and  $\omega_z'$  are positively correlated, consistent with Lighthill's mechanism. Klewicki *et al.* (1994) interpreted this result apparently somewhat differently in terms of low-speed streaks with u' < 0,  $\omega_z' > 0$  moving upward with v' > 0, and high-speed streaks with u' > 0,  $\omega_z' < 0$  moving downward with v' < 0. However, these observations are not inconsistent with Lighthill's argument (see especially the remarks at the end of this subsection and Figs. A.1-A.2 in the Supplementary Materials). Klewicki *et al.* (1994) observed also that  $\langle v'\omega_z' \rangle < 0$  for  $y^+ > 10$  with the main contributions from quadrants  $Q^+$ 4 and especially  $Q^+$ 2 of the PDF  $Q^+$ 4 of the PDF  $Q^+$ 5, and they explained this down-gradient transport in essentially the same manner as we have.

The partial averages of the stretching contribution  $-w\omega_y$  to vorticity flux plotted in Fig. 7c show diametrically opposite correlations with wall-normal velocity as those for the advection term in the buffer layer, the log layer, and some of the outer layer. The plot shows that in and above the buffer layer inflow is associated with down-gradient flux, while outflow is associated with up-gradient flux (except very near the channel center). This opposite correlation may be explained by the control-volume analysis in the previous section 2 (and Fig. 3), which associates down-gradient flux with the line-stretching mechanism for v' < 0 (shown in Fig. 3a) and up-gradient flux with the corresponding line-compressing mechanism for v' > 0 (shown in Fig. 3b). Here, the outflow (v' > 0) prevails in the combined average, implying that the stretching/tilting term contributes a net up-gradient flux across the buffer and log layers.

We may explain this once again as a consequence of the near-equality of spanwise velocity magnitudes |w| for the two conditions but with wall-normal vorticity magnitude  $|\omega_y|$  larger nearer the wall and smaller further away. Note that inflow and outflow are both associated with up-gradient vorticity flux from the stretching/tilting term for  $y^+ < 15$ . The outflow term makes the larger contribution, which is now augmented by a smaller contribution from the inflow.

It may be relevant here that all nonlinear vorticity flux terms vanish identically at the channel wall. Thus, growth on average of spanwise vorticity in this very near-wall region must be due to nonlinear flux of vorticity inward, because the nonlinear flux outward must be small. The vortex lines in this region tend also to be strongly aligned in the spanwise direction, so that the geometry assumed in the control-volume argument is not typical here. Brown *et al.* (2015) investigated the buffer-layer statistics of  $w\omega_y$  by a DNS nearly identical to ours and their Figure 4 plots vortex lines originating at  $y^+ = 10$  in the vicinity of a quasi-streamwise vortex. They argued that such coherent streamwise vortices are responsible for creating the "up-gradient" correlation  $\langle w\omega_y \rangle < 0$  in the buffer layer, because vortex lines

on the side where v>0 are lifted into  $\Lambda$ -shape with converging legs, while lines on the v<0 side are depressed into U-shape with diverging legs. Note that this explanation agrees with our observation in Fig. 7c that partial averages of  $w\omega_y$  are negative both for v>0 and for v<0 in the buffer layer. Brown *et al.* (2015) anticipated also our result that the partial average for v>0 should exceed that for v<0, arguing that  $\omega_y$  magnitudes for v<0 will be weakened by creation of image vorticity at the wall. It is worth emphasizing a further numerical finding of Brown *et al.* (2015) that the pointwise values of  $w\omega_y$  at v=0 have a strongly non-Gaussian PDF giving high probability to events with magnitudes v=0 larger than the mean, so that the overall negative value v=0 in the buffer layer results from near-cancellation between much larger contributions of opposite signs.

A key conclusion of all three of our Figs. 7a-7c is that the net effects seen in the partial averages of the total nonlinear flux in Fig. 7a are due to the dominance of the advection term. Thus, of the two effects considered in the control-volume analysis in section 2, the advective contribution generally outweighs the stretching/tilting contribution. The opposing nature of the partial averages for the advection and stretching/tilting terms in the buffer and log layers, in addition to the correlations with inflow and outflow, strongly support Lighthill's idea of inflow being correlated with stretching/strengthening and outflow with compression/weakening of vortex lines, thereby providing a posteriori validation of the theory.

It might appear paradoxical at first glance that inflow dominates in the total nonlinear flux for the region  $y < y_p$ , while outflow dominates in the two separate flux contributions from advection and stretching/tilting in and above the buffer layer, including a region where  $y < y_p$ . However, the advection and stretching/tilting contributions oppose each other in this region and the outflow contributions suffer more cancellation in the combined flux than do the inflow contributions. In particular, the down-gradient flux from the stretching term during inflow is comparatively weak. In the viscous sublayer, where the control volume analysis of section 2 does not apply, the inflow contribution to the stretching/tilting term is again weaker than the outflow contribution but both are now up-gradient, together with the net advective flux. The Lighthill (1963) mechanism is consistent with these observations. In order to make an objective assessment of the evidence we have investigated other possible correlations as well. However, none of these alternative correlations presented such a clear picture as the correlations with outflow/inflow. Thus, we present these alternative correlations in the Supplementary Materials for completeness. For example, we considered partial averages of the three flux terms  $v\omega_z - w\omega_y$ ,  $v\omega_z$ , and  $-w\omega_y$  conditioned on "low-speed" (u' < 0) and "high-speed" (u' > 0) events (Meinhart & Adrian 1995; Kim & Adrian 1999; Hwang et al. 2016; Hwang & Sung 2018), as shown in Fig. A.1 of the Supplementary Materials. While there is a clear correlation of the advective term (down-gradient for low speed and up-gradient for high speed, consistent with Klewicki et al. (1994)), the stretching term is found to be insensitive to the conditions u' > 0 and u' < 0. Perhaps the most interesting of these additional correlation studies involved the standard quadrant analysis of the Reynolds stress (Willmarth & Lu 1972; Lu & Willmarth 1973; Bogard & Tiederman 1986; Pope 2000; Lozano-Durán et al. 2012). As shown in Fig. A.2 of the Supplementary Materials, the partial averages of the flux terms conditioned on Q2-events (u' < 0, v' > 0) or "ejections" are very similar to those conditioned on v' > 0 alone, and those conditioned on O4 events (u'>,v'<0) or "sweeps" are very similar to those for v'<0 alone. By contrast, the partial averages for  $Q_1$  and  $Q_3$  events are distinctly smaller in magnitude. The relevant conclusion is that much of the vorticity flux correlations observed in this section with outflow and inflow events arise from the corresponding "active" regions of the flow, Q2 and Q4, which contribute also to the Reynolds shear stress. See Vidal et al. (2018) for related results discussed more in the Supplemental Materials, section A.

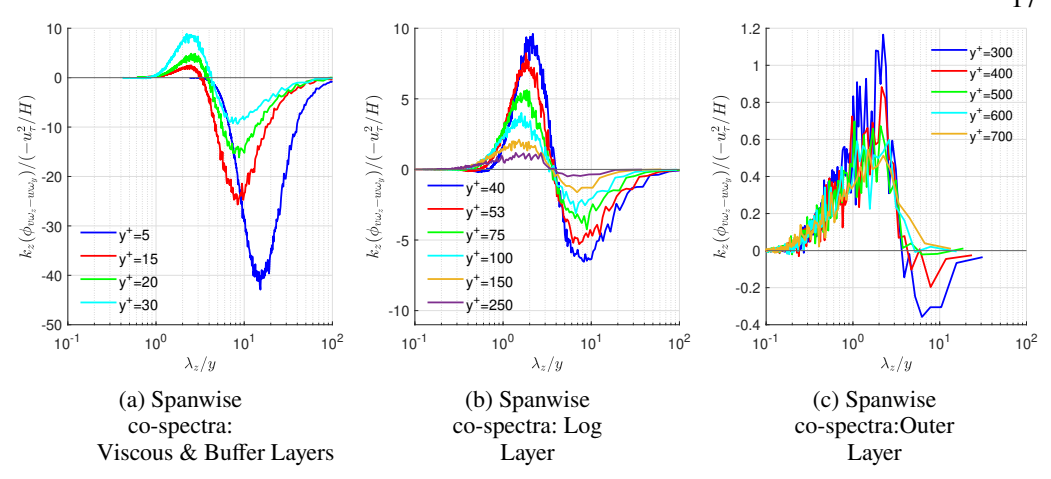


Figure 8: Normalized spanwise cospectra of the nonlinear term, in the (a) viscous & buffer layers, (b) log layer and (c) outer layer. Here, the abscissa shows wavelength divided by y.

## 3.3. Velocity-vorticity cospectra

The main prediction of the Lighthill (1963) theory is up-gradient vorticity transport toward a solid wall, with eddy contributions naturally depending upon the size of eddies relative to the wall distance y. Since the theory posits strong spanwise stretching, the vorticity transport effects should be particularly sensitive to the spanwise extent of eddies. This motivates us to consider the 1-D spanwise vorticity-flux co-spectrum  $\phi_{v\omega_z-w\omega_y}(k_z)$  which gives the net contribution of eddies with spanwise wavenumber magnitude  $k_z$  or corresponding wavelength  $\lambda_z = 2\pi/k_z$ . Such a co-spectrum may defined for any direction of homogeneity (x, z), or a linear combination thereof) by taking FFTs of velocity and vorticity, followed by an inner product, and averaging in time over snapshots and along the orthogonal homogeneous direction. The cospectrum so defined yields a spectral decomposition of the nonlinear vorticity flux:

$$\int_0^\infty \phi_{v\omega_z - w\omega_y}(k_i, y) dk_i = \langle v\omega_z - w\omega_y \rangle(y), \ k_i = k_x \ or \ k_z.$$
 (3.3)

The co-spectra are closely related to the "net force spectra", defined as the wall-normal derivative of the Reynolds shear stress co-spectra discussed in prior works of Guala et~al. (2006), Balakumar & Adrian (2007) and Wu et~al. (2012). Similar cospectra  $\phi_{v\omega_z}(k_i,y)$ ,  $\phi_{w\omega_y}(k_i,y)$  can be defined for the individual velocity-vorticity correlations  $\langle v\omega_z \rangle(y)$  and  $\langle w\omega_y \rangle(y)$ , with prior empirical studies of Priyadarshana et~al. (2007) and Morrill-Winter & Klewicki (2013) having calculated individual streamwise cospectra as well. Azimuthal cospectra were calculated by Wu et~al. (2012) for pipe flows. These were calculated as a function of the azimuthal angle and are somewhat similar to spanwise co-spectra for pressure-driven channel flows. However, we are aware of no prior studies which directly compute this quantity for channel flows. Therefore, we have validated our calculations by comparing our results with the corresponding spatial two-point velocity-vorticity correlations in the spanwise direction obtained from channel flow DNS at  $Re_\tau = 934$  by Del Alamo et~al. (2004), as reported in Monty et~al. (2011). This comparison, shown in Fig B.3 in the Supplementary Materials, confirms our own data presented here.

We plot in Fig. 8 the spanwise flux cospectra for several y values each in the buffer layer, log-layer and outer layer. To make the results more physically intuitive, we have plotted the cospectra versus  $\lambda_z/y$  in log-scale and then compensated by the factor  $k_z = 2\pi/\lambda_z$  necessary

to yield the correct total integrals. We have further normalized by the asymptotic value  $-u_{\tau}^2/H$  achieved by the mean nonlinear flux  $\langle v\omega_z - w\omega_y \rangle(y)$  for  $y \gg y_p$ . With the latter normalization, positive values of the cospectra count as "down-gradient" and negative as "up-gradient." The most striking feature of the results plotted in Fig. 8 is the existence of a precise spanwise length scale  $\lambda_z^*$  such that the cospectrum is "down-gradient" for  $\lambda_z < \lambda_z^*$  and "up-gradient" for  $\lambda_z > \lambda_z^*$ . Furthermore,  $\lambda_z^*$  is proportional to y,  $\lambda_z^* \doteq \gamma y$  with a prefactor  $\gamma = 3 \sim 4$  over the entire range of y-values; see also the plot of  $\lambda_z^*$  vs. y in Figure 9. Physically, it is the eddies with spanwise wavelengths  $\lambda_z$  greater than  $\gamma y$  that are subjected to the correlated inflow and spanwise stretching proposed by Lighthill (1963), whereas the eddies with  $\lambda_z$  less than  $\gamma y$  instead transport vorticity down-gradient away from the wall. To compare  $\lambda_z^*$  with other relevant length scales in wall-bounded flow, note that the integral length given nominally by  $\ell = \kappa y$  for von Kármán constant  $\kappa \doteq 0.4$  is about 10 times smaller. Nickels et al. (2005) have estimated that the "production range" of attached eddies with  $k_x^{-1}$ energy spectrum occurs for 15.7y  $< \lambda_x < 0.3H$ . If we adopt the relation  $\lambda_z \sim \lambda_x/7$  suggested by results for 2D energy spectra in  $(k_x, k_z)$  (Chandran et al. 2017), then this production range corresponds to  $\lambda_z > 2.24y$  and includes the "up-gradient" scales  $\lambda_z > (3 \sim 4)y$  identified by our results. However, we shall present concrete evidence later that the up-gradient vorticity flux is not associated to wall-attached eddies. Although the normalized flux cospectra plotted in Figure 8 all pass through zero at  $\lambda_z/y = 3 \sim 4$ , their integrals over  $\log(\lambda_z/y)$  must shift from negative values for y in the buffer layer, pass through zero at  $y = y_p$ , and then approach 1 for  $y \gg y_p$ , consistent with the results for  $\langle v\omega_z - w\omega_y \rangle(y)$  plotted in Figure 5. This change in the integrated values occurs via a shift between the two halves of the cospectrum with increasing y, whereby the negative "up-gradient" branch at  $\lambda_z > \lambda_z^*$  dominates in the buffer layer but diminishes with increasing y as the positive "down-gradient" branch at  $\lambda_z < \lambda_z^*$ increases. This increase of the down-gradient branch relative to the up-gradient branch continues in the log-layer, with the two coming into exact balance at  $y = y_p = 53$ . However, unlike the buffer layer, increasing distance from the wall in the log layer sees a decrease in the magnitude of both down-gradient and up-gradient branches. For y further increasing into the outer layer, the up-gradient branch at  $\lambda_z > \lambda_z^*$  continues to diminish and the down-gradient branch at  $\lambda_z < \lambda_z^*$  stabilizes to a positive cospectrum independent of y. At the extremes, for  $y^+ \lesssim 10$  there is essentially no down-gradient branch and for  $y^+ \gtrsim 500$  no up-gradient branch. Physically, the eddies for  $y^+ \gtrsim 500$  (or  $y \gtrsim 0.5H$ ) no longer feel the effect of the wall. These results for the flux cospectrum highlight the delicate balance between competing fluxes proposed by Lighthill (1963) and restated in Sec 1. The remarkable persistence of  $\lambda_z^*/y = 3 \sim 4$  lends credence to Lighthill's idea that the up-gradient transport of vorticity towards the wall is a scale-by-scale cascade process (see Sec 1), since  $\lambda_z^*$  can be viewed as the "smallest" up-gradient spanwise scale which gets smaller  $\propto y$  as vorticity is transported nearer to the wall.

The intense competition between nonlinear vorticity transport in opposite directions arising from different scales of motion, vividly illustrated in Figure 8, implies that the net "downgradient" transport for  $y > y_p$  must arise from scales much smaller than y and likewise the net "up-gradient transport" for  $y < y_p$  must arise from scales much larger than y. In order to quantify the extent of cancellation between co-spectral regions with opposing fluxes, we define the fractional cumulative flux

$$f(y,\Lambda) = \begin{cases} \frac{1}{\langle v\omega_z - w\omega_y \rangle(y)} \int_{2\pi/\Lambda}^{\infty} \phi_{v\omega_z - w\omega_y}(k_z, y) dk_z, & \text{if } y < y_p \\ \frac{1}{\langle v\omega_z - w\omega_y \rangle(y)} \int_0^{2\pi/\Lambda} \phi_{v\omega_z - w\omega_y}(k_z, y) dk_z, & \text{if } y > y_p \end{cases}$$
(3.4)

which for  $y < y_p$  measures the fraction of nonlinear vorticity flux arising from wavelengths  $\lambda_z < \Lambda$  and for  $y > y_p$  measures the fraction arising from  $\lambda_z > \Lambda$ . One important spanwise

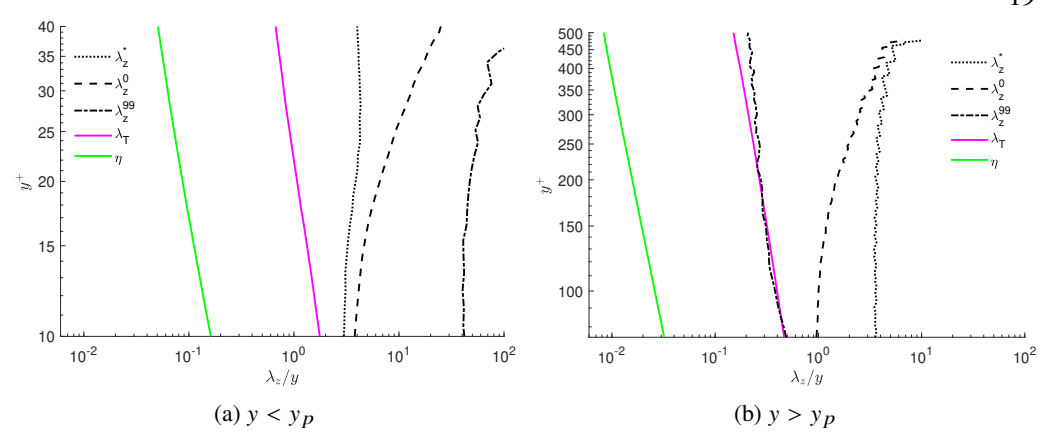


Figure 9: Characteristic spanwise wavelengths relevant to nonlinear vorticity transport, defined based on Eq. 3.4, for (a)  $y < y_p$  and (b)  $y > y_p$ .

scale which may be defined in the range  $10 \lesssim y^+ \lesssim 500$  where two opposite-signed branches of the cospectrum co-exist is the "break-even" wavelength  $\lambda_z^0$  satisfying  $f(y, \lambda_z^0) = 0$ . For  $y < y_p$  spanwise scales as large as  $\lambda_z^0 > \lambda_z^*$  must be included to get exactly cancelling flux, and for  $y > y_p$  spanwise scales as small as  $\lambda_z^0 < \lambda_z^*$  must be included to get cancelling flux. Perhaps even more relevant is the "99%" wavelength  $\lambda_z^{99}$  satisfying  $f(y, \lambda_z^{99}) = 0.99$ . According to this definition, spanwise scales as large as  $\lambda_z^{99} > \lambda_z^0$  must be included to get 99% of the net up-gradient flux for  $y < y_p$ , and spanwise scales as small as  $\lambda_z^{99} < \lambda_z^0$  must be included to get 99% of the net down-gradient flux for  $y > y_p$ . Note that at  $y = y_p$ , the cospectrum integrates to zero, and hence  $\lambda_z^0 \to \infty$  and  $\lambda_z^{99} \to \infty$  as  $y \to y_p$ , for  $y < y_p$ . And,  $\lambda_z^0 \to 0$  and  $\lambda_z^{99} \to \infty$  as  $y \to y_p$ , for  $y > y_p$ . Therefore, these scales do not have meaningful physical interpretations close to  $y_p$ , while they provide useful information viz. the scales yielding nonzero nonlinear flux. All of the length-scales  $\lambda_z^*$ ,  $\lambda_z^0$  and  $\lambda_z^{99}$  are plotted together versus  $y^+$  for  $10 < y^+ < 40$  in Fig. 9a and for  $75 < y^+ < 500$  in Fig. 9b, corresponding to  $y < y_p$  and  $y > y_p$  respectively. For  $y < y_p$  (9a) the plotted results show that  $\lambda_z^{99}$  begins as 40y in the buffer layer and increases to more that 100y approaching  $y^+ = 40$ , making manifest the very large spanwise scales involved in Lighthill's "up-gradient" mechanism. We have also added for reference to Fig. 9 two characteristic turbulent small scales, the Kolmogorov scale  $\eta$  and the Taylor scale  $\lambda_T$ . Here we have followed standard definitions  $\eta = v^{3/4} \epsilon^{-1/4}$  and  $\lambda_T = [5v(u_{rms}^2 + v_{rms}^2 + w_{rms}^2)/\epsilon]^{1/2}$ , estimating energy dissipation as  $\epsilon = P_K/\alpha$  in terms of turbulence production  $P_K = -\langle u'v'\rangle\partial_y U$  and the factor  $\alpha$  from Figure 7 of Lee & Moser (2015). Note, that the scales associated with up-gradient flux  $(\geq \lambda_z^*)$  are at least one order of magnitude larger than the Kolmogorov scale, where streamwise organization associated with stronger spanwise scales can be expected. Remarkably, for  $y > y_p$  (9b) in the log layer we see that  $\lambda_z^{99} \doteq \lambda_T$  to a very good approximation and in the outer layer  $\lambda_z^{99}$  is only a factor of a few times larger than  $\lambda_T$ . Thus, we conclude that fine-scale eddies with spanwise wavelength  $\lambda_T$ down to nearly the Taylor microscale contribute significantly to the down-gradient transport of vorticity at  $y > y_p$ . Similar observations were made previously by Priyadarshana et al. (2007) based on streamwise cospectra  $\phi_{v\omega_z}(k_x, y)$ ,  $\phi_{w\omega_y}(k_x, y)$  (see further below). The sensitivity of the nonlinear vorticity transport to such small scales for  $y > y_p$  has important implications for physical phenomena such as polymer drag-reduction since modifications of the flux cospectrum at very small scales can alter the delicate balance between down-gradient



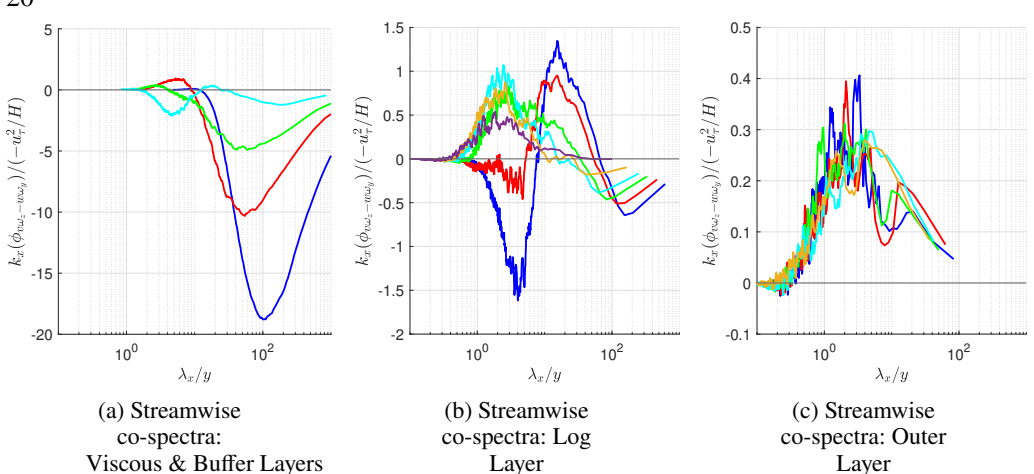


Figure 10: Normalized streamwise co-spectra of the nonlinear term  $(\phi_{V\omega_z} - \phi_{W\omega_y})$ , in (a) the viscous & buffer layers, (b) log layer and (c) outer layer. Different curve colors represent different distances from the wall within each of the three layers, as in corresponding plots in Fig 8.

and up-gradient transport and lead to a drastic reduction of drag (cf. Crawford & Karniadakis (1997); Monty *et al.* (2011)).

We have calculated as well the separate spanwise cospectra for the advective flux  $\phi_{v\omega_z}(k_z,y)$ , and the stretching flux  $-\phi_{w\omega_y}(k_z,y)$ . These contain less information than the cospectrum of the total nonlinear flux, so we just briefly summarize here the key observations and relegate the plots of those cospectra to Fig C.4 and Fig C.5 in the Supplementary Materials. Most significantly, the stretching cospectrum is predominantly "up-gradient" for all  $y^+$  values and the advective cospectrum predominantly "down-gradient" for  $y^+ > 5$ . Intriguingly,  $\phi_{v\omega_z}(k_z,y)$ , switches sign for  $y^+ \le 10$ , where it becomes almost entirely "up-gradient". These signs are all consistent with those of the mean values  $\langle v\omega_z \rangle(y)$  and  $-\langle w\omega_y \rangle(y)$  plotted in Fig. 5 and the underlying physical mechanisms are presumably the same as discussed in that connection. A relevant conclusion is that in Fig. 8 the "down-gradient" branch in the nonlinear flux cospectrum  $\phi_{v\omega_z-w\omega_y}(k_z,y)$  arises mainly from advection, whereas the "up-gradient" branch arises mainly from stretching.

We have studied in addition the streamwise cospectra  $\phi_{v\omega_z}(k_x, y)$ ,  $-\phi_{w\omega_y}(k_x, y)$ , and  $\phi_{V\omega_z-W\omega_y}(k_x,y)$ , but we have found that these present a much less clear physical picture and are not as easily interpretable as the spanwise cospectra. We thus present here in Fig. 10 only the streamwise cospectra for the total nonlinear flux, which may be directly compared with the spanwise cospectra in Fig. 8, and we relegate to the Supplementary Materials in Figs. C.6, C.7 the cospectra for advective and stretching fluxes. The latter are shown to agree qualitatively with prior experimental results of Priyadarshana et al. (2007); Morrill-Winter & Klewicki (2013) at somewhat different Reynolds numbers and for boundary layers. Referring briefly to the results plotted in Fig. 10, we remark that the streamwise cospectra at  $y^+ = 5$  and  $y^+ = 15$  shown in Fig 10a are qualitatively similar to the corresponding spanwise cospectra. However, as y<sup>+</sup> increases to 30, the streamwise cospectrum develops a region of down-gradient behaviour (at  $\lambda_x \sim 10y$ ) sandwiched between regions of upgradient behaviour (at  $\lambda_x \sim 4y$  and  $\lambda_x \sim 200y$ ). Such behaviour persists into the log layer until reaching  $y^+ = 53$  (shown in Fig 10b) whereupon the behaviour changes again to qualitatively resemble spanwise spectra with down-gradient contributions from  $\lambda_x < \lambda_x^*$  and up-gradient contributions from  $\lambda_x > \lambda_x^*$  (as seen at  $y^+ = 75 - 250$ ). Here,  $\lambda_x^*$  is the streamwise

wavelength at which the co-spectrum crosses the x-axis. However, streamwise cospectra do not possess the persistent and sharp boundary between competing fluxes across the log layer seen in the spanwise case and  $\lambda_x^*/y$  varies significantly with y. At  $y^+ = 250$  and into the outer layer (Fig 10c), the streamwise cospectra are purely down-gradient. The streamwise and spanwise cospectra are naturally similar near the center line due to the larger degree of component isotropy there. We also remark that streamwise net force spectra have been the subject of detailed study in prior works of Guala et al. (2006); Balakumar & Adrian (2007); Wu et al. (2012). In these works, the wall-normal derivative of the Reynolds shear stress is characterized as producing retardation of the mean flow above  $y_p$  and acceleration below, associated in their study with a negative and a positive sign respectively. This retarding force is produced by a down-gradient flux of spanwise vorticity while an accelerating force results from an up-gradient flux, as discussed in Sec 1(see also, Eyink (2021)). A detailed study by Wu et al. (2012) finds large positive (accelerating) values for the streamwise net force spectrum concentrated below  $y^+ = 20$ , and observes that below the top of the buffer layer (at  $y^+ = 30$ ), all scales except the very smallest ( $\lambda_x < 0.15R$ ,  $R^+ = 685$ ) accelerate the mean flow (or contribute an up-gradient flux). Conversely, for y > 0.2R, they find negative (decelerating or contributing a down-gradient flux) values for all scales. In the wall-normal region where  $y^+ > 20$  and y < 0.2R, they find a complicated y variation of the spectra with negative (decelerating or with a down-gradient flux) values sandwiched between positive (decelerating or with an up-gradient flux) values, each occupying a varying range of scales. These observations mirror our own, as illustrated particularly by Fig 10.

Following the approach of Wu *et al.* (2012) for pipe flows, the somewhat complicated picture arising from the streamwise cospectra is clarified by studying, the 2D cospectra in  $(k_x, k_z)$ , which provide more detailed information about the different scales of motion in streamwise and spanwise directions simultaneously. Cospectra are calculated by computing 2D FFTs of velocity and vorticity, followed by taking appropriate inner products and averaging in time. We also added contributions reflected in the x- and z-axes so that the spectra depend only on wavelength magnitudes  $k_x \ge 0$ ,  $k_z \ge 0$ , yielding the following spectral decomposition of the nonlinear vorticity flux:

$$\int_0^\infty \int_0^\infty \varphi_{v\omega_z - w\omega_y}(k_x, k_z, y) \ dk_x \ dk_z = \langle v\omega_z - w\omega_y \rangle(y) \tag{3.5}$$

Because the 2D cospectra were obtained by averaging over only 38 snapshots, rather sizable fluctuations remained in the results. Thus, to obtained more converged results, we smoothed these cospectra using 2D running averages in Fourier space. The smoothing based on the Principle of Minimal Sensitivity (Stevenson 1981) is discussed fully in the Supplementary Materials, section D, but we note here that the smoothing employed preserves the total integral in Eq. (3.5) and that the cospectra plotted in Fig. 11 are relatively insensitive to the exact choice of filter width  $\Delta k$  in the range considered. We have also chosen to plot the 2D spectra versus normalized wavelengths  $\lambda_x/y$  and  $\lambda_z/y$ , both in log-scale and compensated by the factor  $k_x k_z$  to yield the correct double integral over  $(\log(\lambda_x/y), \log(\lambda_z/y))$ . We have again normalized by the factor  $-u_{\tau}^2/H$ , so that positive values represent down-gradient transport and negative values up-gradient. We plot 2D cospectra for three y-values each in the viscous sublayer and buffer layer (Fig. 11a-11c), the log layer (Fig. 11d-11f), and outer layer (Fig. 11g-11i)). The most important feature of the 2D spectra is that, like the 1D spanwise spectrum but unlike the streamwise spectrum, there is a clear bipartite structure, with two distinct branches or "lobes", with clear spectral boundaries, corresponding to the competing down-gradient and up-gradient transport. In fact, these boundaries are mainly along the line  $\lambda_z/y = 3 \sim 4$  but with also another boundary depending upon  $\lambda_x$  for  $\lambda_z/y \gtrsim 3 \sim 4$ . These results illuminate why the 1D streamwise cospectra do not yield a clear bipartite structure

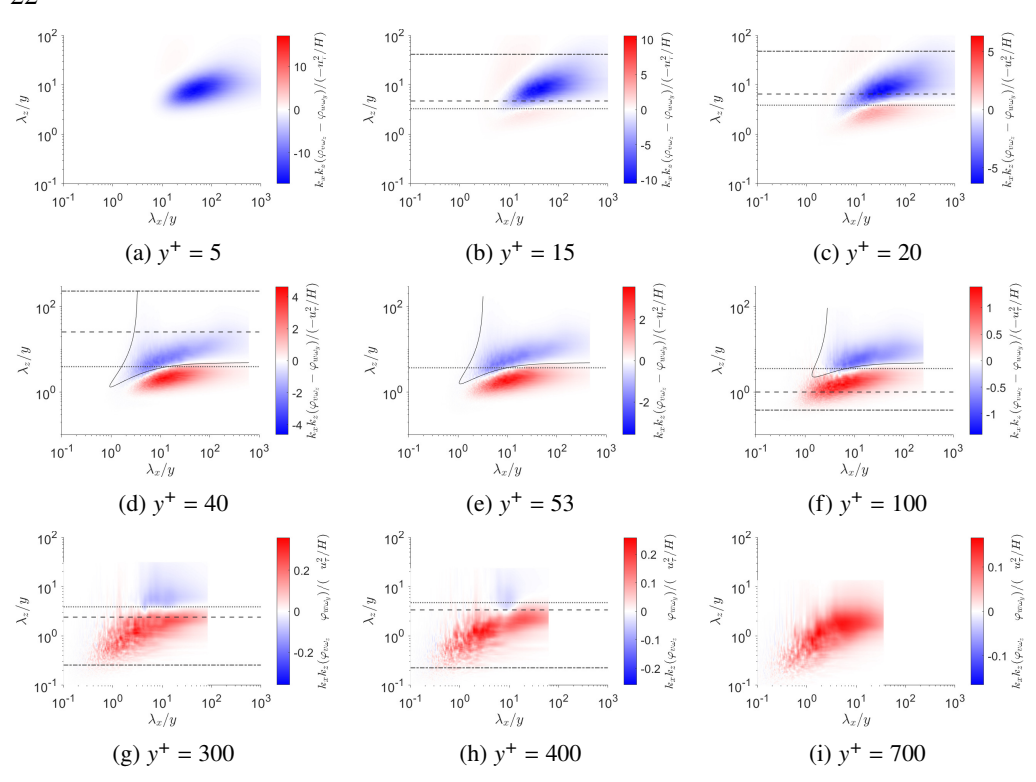


Figure 11: Normalized compensated 2D co-spectra of the nonlinear flux  $\varphi_{V\omega_z-W\omega_y}(k_x,k_z,y)$ , in the viscous & buffer layers (a,b,c), log layer (d,e,f), and outer layer (g,h). The solid curves mark the iso-contour of the filter  $\mathcal{D}(k_x,k_z,y)=0.5$ , described in Supplementary Materials F. The dotted, dashed and dashed-dot lines represent  $\lambda_z^*$ ,  $\lambda_z^0$  and  $\lambda_z^{99}$  respectively, as in Fig 9.Note that the range of a color-bar does not reflect the actual range of values of the spectrum since only one color achieves saturation while the other does not. For example, spectrum (c) ranges from -6.4 to 2.5 while (g) ranges from -0.11 to 0.36.

after integration over  $k_z$ , while integration over  $k_x$  preserves such structure. A main new implication of the 2D cospectra is that up-gradient transport requires not only  $\lambda_z/y \gtrsim 3 \sim 4$  but also  $\lambda_x/y \gtrsim 3 \sim 4$ , or even larger.

We now comment briefly on significant features and consequences of the 2D cospectra for the various wall distances.

In the viscous sublayer and buffer layer, the dominant up-gradient contribution to the nonlinear flux corresponds to the blue region in Fig. 11a-11c, which is characterized roughly by  $\lambda_z/y \gtrsim 3$  and  $\lambda_x \gtrsim \lambda_z$ . The competing down-gradient contribution indicated by red color is weaker and in the viscous sublayer at  $y^+ = 5$  it is almost entirely negligible. The peak negative value of the cospectra associated to up-gradient transport occurs around wavelengths  $(\lambda_x, \lambda_z) \sim (30y, 8y)$ , whose ratio is indicative of sublayer streaks. These are the type of flow structures "elongated in the stream direction" mentioned by Lighthill (1963) and whose relevance to near-wall vorticity transport has been discussed in several previous studies (Klewicki *et al.* (1994); Brown *et al.* (2015); Arosemena & Solsvik (2022)).

In the log-layer, the contributions to down-gradient and up-gradient transport from the 2D cospectra plotted in Fig. 11d-11f are more nearly in balance, with an exchange of dominance at  $y = y_p$ . The blue portion associated with up-gradient transport occupies very

crudely the region specified by the two constraints  $\lambda_z/y \gtrsim 4$  and  $\lambda_x/y \gtrsim 4$ , requiring large wavelengths in both spanwise and streamwise directions. (The black curves in Fig. 11d-11f plot more precise boundaries of this region. The aim to separate the flow into contributions on either side of these lines motivates us to define a filter, termed the "dragonfly filter" due to its shape once the black line is mirrored to all four quadrants. The dragonfly filter is discussed in more detail in §3.4 and in the Supplementary Materials F.) The red portion of the cospectrum associated to down-gradient transport obtains most of its contribution, on the other hand, from the region with  $\lambda_z/y \lesssim 4$  but with  $\lambda_x/y$  ranging over values both much smaller and larger than unity. As y increases, this down-gradient spectral region extends to smaller  $\lambda_x/y$  and  $\lambda_z/y$ , and simultaneously the position of peakpositive cospectrum shifts to smaller wavelengths. The negative, up-gradient portion of the cospectrum instead peaks around  $(\lambda_x/y, \lambda_z/y) \sim (10, 10)$  for all y. These observations imply not only that the down-gradient transport becomes more dominant with increasing y but also that it originates from an increasing range of spanwise and streamwise scales, down to the Taylor microscale Priyadarshana et al. (2007). Meanwhile, the up-gradient contributions arise only from spanwise and streamwise scales larger than the integral scale and with dimishing magnitudes at greater wall distances.

These trends with increasing y continue for the 2D cospectra in the outer layer plotted in Fig. 11g-11i. The up-gradient spectral region continues to be specified roughly by  $\lambda_z/y \gtrsim 4$  and  $\lambda_x/y \gtrsim 4$ , but the cospectrum magnitudes in this sector drop rapidly with y. For  $y^+ \gtrsim 500$  the up-gradient contribution is essentially negligible and only the down-gradient contribution from the small scales remains. The cospectra for the latter have furthermore shifted to even smaller values of  $\lambda_z/y$  and  $\lambda_x/y$ . Additionally, we have marked  $\lambda_z^*$ ,  $\lambda_z^0$  and  $\lambda_z^{99}$  on the cospectra, also plotted in Fig. 9. For  $y < y_p$  (Fig.11b-11d), the part of the co-spectrum below the dashed line  $(\lambda_z^0)$  integrates to zero, and 99% of the (up-gradient) flux comes from the region between the dashed and the dot-dashed line  $(\lambda_z^{99})$ . Similarly, For  $y > y_p$  (Fig.11f-11h), the part of the co-spectrum above the dashed line  $(\lambda_z^0)$  integrates to zero, and 99% of the (down-gradient) flux comes from the region between the dashed and the dot-dashed line  $(\lambda_z^{99})$ .

Wu et al. (2012) also observe a similar bipartite structure in their plots of 2D net force spectra for pressure-driven pipe flows (shown in Figure 18 of their paper). They find that the spectra at all considered y values are similar in that each posses an ellipse of negative net force (decelerating or with a down-gradient flux contribution) below (at shorter azimuthal wavelengths) an ellipse of positive net force (accelerating or with an up-gradient flux contribution) while occupying similar streamwise scales. The combined effect of all azimuthal scales leads to the complex behavior of the  $\lambda_x$  spectra, while integrating over streamwise scales leads to azimuthal spectra (a function of  $\lambda_{\theta}$ , where  $\theta$  is the azimuthal angle) with a consistent pattern of behavior, reflecting the structure of the 2D spectra. Since their azimuthal spectra possess a negative (decelerating or down-gradient) region for small scales and a positive(accelerating or up-gradient) region at larger scales, we can mark the wavelength  $\lambda_{\theta}^*$  at which a spectrum changes sign. We can then calculate  $\lambda_s^* = (R - y)\lambda_{\theta}^*$ , where,  $\lambda_s^*$  is the wavelength defined based on the azimuthal arclength (see also, Figure 11 from Wu et al. (2012) ). The values of  $\lambda_s^*/y$  are compared with  $\lambda_z^*/y$  in Table 1. It is interesting to note that both quantities have only small variations across the different y values considered, especially within the log layer ( $y^+ = 50, 101, 200$ ). The values of  $\lambda_z^*/y$  are at most 22% smaller than  $\lambda_z^*/y$ . This is a high degree of agreement considering that they are for different flow configurations and are at two different Reynolds numbers.

We have calculated also the separate 2D cospectra for the advective flux  $\varphi_{v\omega_z}(k_x, k_z, y)$  and stretching flux  $-\varphi_{w\omega_y}(k_x, k_z, y)$ . These are plotted in Fig. E.10 and Fig. E.11, respec-

```
y^+ \lambda_{\theta}^* \lambda_s^*/y \lambda_z^*/y
20 0.109 3.624 3.866
50 0.234 2.972 3.852
101 0.526 3.040 3.596
200 1.156 2.803 3.621
```

Table 1: Wavelengths  $\lambda_{\theta}^*$  (based on azimuthal angle) and  $\lambda_s^*$  (based on azimuthal arclength) at which the net force spectra change sign, calculated from the azimuthal spectra plotted in Figure 18 of Wu *et al.* (2012), using DNS data of a pressure driven pipe flow at  $R^+ = 685$ . Here  $\lambda_z^*$  is the same as in Figure 9. Here, y is the wall normal distance.

tively, in the Supplementary Materials and here we just summarize their main features. These cospectra have the same bipartite structure as the cospectra for the total nonlinear flux plotted in Fig. 11. The most important difference is that the down-gradient contribution is greatly reduced for the stretching cospectrum in Fig. E.11 and likewise the up-gradient contribution is greatly reduced for the advective cospectrum in Fig. E.10. Thus, the stretching cospectrum contributes primarily up-gradient transport and the advective cospectrum primarily down-gradient transport. The only exceptions to the latter statements are for  $y^+ \lesssim 10$  where the advective cospectrum plotted in Fig. E.10a is almost entirely up-gradient and for  $y^+ \gtrsim 500$  where the stretching cospectrum plotted in Fig. E.11i is almost entirely down-gradient. The other general change in the separate 2D cospectra is that the boundaries between up-gradient and down-gradient transport are slightly shifted, upward to  $\lambda_z/y \simeq 6 \sim 8$  for the advective cospectra in Fig. E.10 and downward to  $\lambda_z/y \simeq 1 \sim 2$  for the stretching cospectra in Fig. E.11. The relevant conclusion for the competing contributions to the nonlinear flux cospectra plotted in Fig. 11 is that the down-gradient contribution arises mainly from advection and the up-gradient contribution mainly from stretching/tilting.

It is informative to compare our results for the 2D flux cospectra in the log layer with those for 2D energy spectra obtained from channel-flow DNS (Del Alamo *et al.* 2004) in the range of Reynolds numbers  $Re_{\tau} = 547 \sim 1901$ , comparable to ours, and also from boundary-layer experiments (Chandran *et al.* 2017, 2020) at much higher Reynolds numbers  $Re_{\tau} = 2430 \sim 26,090$ . It was found by Del Alamo *et al.* (2004) that the  $\lambda_z$  at the maximum of the 2D energy spectrum for each  $\lambda_x$  corresponded to a ridge given by a power-law scaling

$$\lambda_z/y \sim (\lambda_x/y)^p \tag{3.6}$$

with an exponent p = 1/2 that differed from the value p = 1 corresponding to the self-similar structures assumed in the AEM. Chandran *et al.* (2017, 2020) verified this result at their lowest Reynolds numbers but found that for higher  $Re_{\tau}$  the spectral ridge is better fit by a power-law with p > 1/2, especially in the large-scale range  $\lambda_x \geq 20y$ . In the limit of very large Reynolds numbers, they found that  $p \to 1$  and that  $\lambda_z \sim \lambda_x/7$ , consistent with the spectra arising from streamwise elongated but self-similar structures, such as hairpin packets, as assumed in the AEM. Our results for the 2D flux cospectra are strikingly different, becoming almost independent of  $\lambda_x$  for  $\lambda_x/y \geq 10$ . We have quantified this independence by calculating three spanwise wavenumbers  $k_z^u$ ,  $k_z^d$ , and  $k_z^*$  for each streamwise wavelength  $k_x$ , corresponding respectively to the wavenumber where the pre-multiplied cospectrum normalized by  $-u_{\tau}^2/H$  has its minimum (most negative) value, its maximum value, and its zero-crossing, respectively, for that  $k_x$ -slice. The corresponding "ridges" are plotted in Fig. 12a-12c for y = 40, 53, 100 in the log-layer and we find that these are fit reasonably well for  $\lambda_x/y > 30$  by power-laws of the form (3.6), with linear best-fit values given in Table 2. The small values of p quantify how the cospectra become nearly independent of

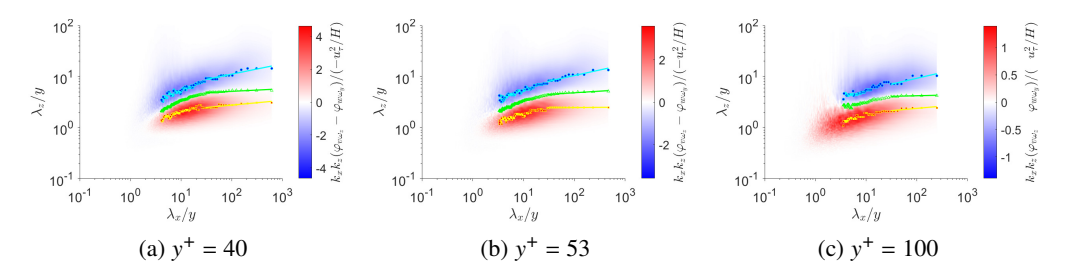


Figure 12: Ridges of spanwise wavelengths  $\lambda_z^u/y$  at minimum cospectrum (blue-filled cyan circles),  $\lambda_z^d/y$  at maximum cospectrum (red-filled yellow squares), and  $\lambda_z^*/y$  at zero cospectrum (green triangles), plotted log-log versus streamwise wavelength  $\lambda_x/y$ , together with the normalized 2D cospectra  $\phi_{v\omega_z-w\omega_y}(k_x,k_z;y)$  for y in the log layer. Power-law fits for the minimum, maximum and zero cospectral ridges at  $\lambda_x \gtrsim 30y$ , are given by cyan, yellow and green lines respectively.

Table 2: Linear fits for  $(\lambda_X/y) \gtrsim 30$ ,  $\lambda_Z^u/y = a_u(\lambda_X/y)^{p_u}$ ,  $\lambda_Z^d/y = a_d(\lambda_X/y)^{p_d}$ ,  $\lambda_Z^*/y = a_*(\lambda_X/y)^{p_*}$ . Here,  $a_u$ ,  $a_d$  and  $a_*$  are constants.

 $\lambda_x$  for wavelengths  $\lambda_x/y \gtrsim 10$ . This finding seems to indicate that the eddies contributing to nonlinear vorticity transport in the log layer are strongly non-self-similar, with  $\lambda_z$  nearly independent of  $\lambda_x$ . This is one piece of evidence that the up-gradient transport proposed by Lighthill (1963) does not arise from attached eddies that are usually assumed to be self-similar. In addition, despite the arguments of Eyink (2008) to the contrary, the results in Fig.12c suggest that for  $y > y_p$  the down-gradient vorticity transport is as well not provided by the self-similar attached eddies assumed in the AEM, at least for  $Re_\tau = 1000$ . In the next section we shall try to clarify this issue by identifying the vortex structures in the flow which are most relevant to the nonlinear vorticity transport.

## 3.4. Coherent vortices and their vorticity flux contributions

There has long been interest in the role of coherent vortex structures in turbulent flows (Cantwell 1981; Hussain 1986; Robinson 1991; Adrian 2007), with new insights related to exact Navier-Stokes solutions that represent such organized states (McKeon 2017; Graham & Floryan 2021). One of the drivers of this sustained attention is the empirical fact that coherent vortices contribute a disproportionate amount to turbulent transport, outsize relative to their small volume fraction in the flow. These considerations have motivated extensive efforts over many years to develop vortex identification methods, with classical methods discussed in prominent reviews (Chakraborty *et al.* 2005; Kolář 2007) and with improved methods continuing to be developed (Haller *et al.* 2016) The bipartite character of the 2D flux cospectrum discussed in the previous subsection provides the basis to investigate the coherent vortex structures which contribute separately to up-gradient and down-gradient vorticity transport. The straightforward idea is to decompose the flow at each y-level into the contributions of two sets of eddies characterized by their support in the 2D Fourier space  $(k_x, k_z)$ , with one field coming from eddies with negative (up-gradient) sign of the

normalized flux cospectrum and the other from eddies with positive (down-gradient) sign. Methods of vortex visualization that have been applied to the full fields can then be applied to the two (nearly) orthogonal fields in order to identify the coherent vortices that contribute most significantly to up-gradient and down-gradient transport.

In Supplementary Materials, section  $\mathbf{F}$  we devise a convenient low-pass filter function  $\mathcal{D}(k_x,k_z,y)$  that selects the spectral region of up-gradient flux, while its complement highpass function  $\mathcal{D}^c(k_x,k_z,y)=1-\mathcal{D}(k_x,k_z,y)$  selects the region of down-gradient flux. The filter functions were chosen to be graded to avoid Gibbs-type oscillations in physical space due to sharp spectral cutoffs. The particular filter function  $\mathcal{D}(k_x,k_z,y)$  that we employ is a Gaussian function with elliptical level sets and with rotation angle relative to the Cartesian axes that depend upon the wall distance y. When extended to the space of signed wavenumbers by reflections in the Cartesian coordinate axes, the levels of this function (see Fig. F.13a) resemble the crossed wings of a dragonfly and hence we have dubbed this function the "dragonfly filter". In the other panels of Fig. F.13 in the Supplementary Materials we illustrate how this filter selects regions of negative normalized flux cospectrum. All spatial fields q(x,y,z) such as velocity and vorticity are then filtered by taking 2D FFT's, multiplying by  $\mathcal{D}(k_x,k_z,y)$  or  $\mathcal{D}^c(k_x,k_z,y)$ , and then taking a 2D inverse FFT to obtain two fields, the contributions  $q^U(x,y,z)$  of "U-type eddies" and  $q^D(x,y,z)$  of "D-type eddies". We can then calculate separate nonlinear fluxes  $\Sigma_{yz}^F := v^F \omega_z^F - w^F \omega_y^F$  for both F = U, D. Since off-diagonal terms such as  $v^U \omega_z^D$  are small after averaging over both x and z, this yields a nearly additive decomposition for averages  $\langle \Sigma_{yz}^{nlin} \rangle \doteq \langle \Sigma_{yz}^U \rangle + \langle \Sigma_{yz}^D \rangle$ .

We begin with a discussion of the coherent vortices for the high-pass field  ${\bf u}^D$ , identified based on the discriminant function  $\lambda_D$ . These structures are plotted in Fig 13 and shall be referred to here as "D-type vortices" since they arise from the field  ${\bf u}^D$  which accounts for the down-gradient nonlinear vorticity flux away from the wall. We visualize here only the vortices in the log-layer of the simulation, corresponding to  $30 < y^+ < 300$ . The vortex surfaces in the figure are colored based on the pointwise values of the down-gradient flux  $\Sigma_{yz}^D$ . The most immediate observation about the D-type vortices is that they have a very similar morphology to the well-known "hairpin vortices" that have been frequently visualized in the full velocity field  ${\bf u}$  of turbulent wall-bounded flows, not only by the  $\lambda_2$ -criterion (Jeong  ${\it et al.}$  1997) but also by alternative methods such as swirling strength (Adrian & Liu 2002; Alfonsi  ${\it et al.}$  2011) and the  ${\it Q}$ -criterion (Wu & Moin 2009). We note that most of these vortices are "prograde" with  $\omega_z < 0$  and "retrograde" vortices with  $\omega_z > 0$  are greatly outnumbered. Many of the hairpins also appear to be strongly asymmetric, with one much weaker leg, in

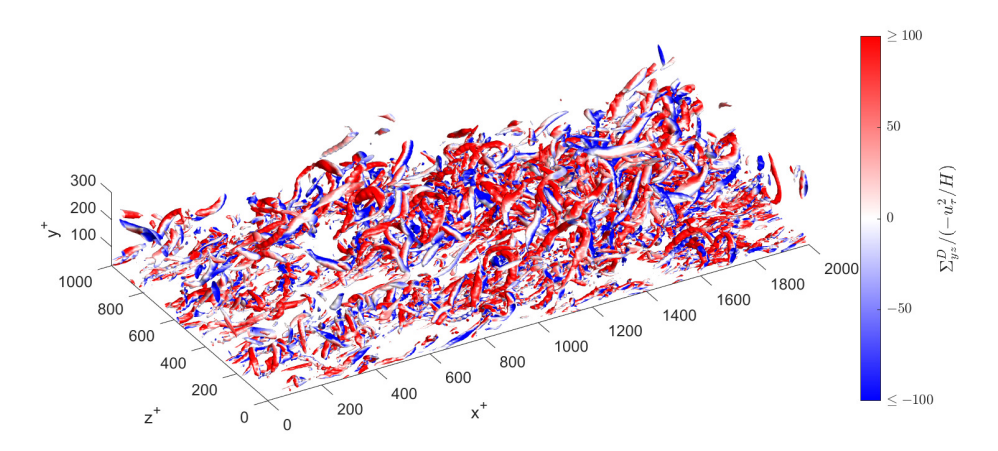


Figure 13: Vortices identified using the  $\lambda_2$ -criterion for the velocity field  $\mathbf{u}^D$  filtered using  $\mathcal{D}^c$ . Isosurfaces are plotted for  $\lambda_2^D = -\lambda_2^{D,rms}$  and coloured by the nonlinear flux  $\Sigma_{yz}^D$ . The three dimensional figure is available at http://cocalc.com/.../D-vortices.html. The data and code to generate such 3D vortices are available at http://cocalc.com/.../3D-vortices/.

agreement with some previous observations (Adrian 2007). Hairpin vortices or packets of hairpins are often considered to be plausible candidates for the "attached eddies" in the AEM (Adrian 2007; Marusic & Monty 2019). Although we attempt here no detailed statistical analysis, the D-type vortices pictured in Fig 13 appear indeed to be wall-attached structures, with feet of one or both legs planted in the near-wall region. These observations agree with the suggestion of Eyink (2008) and others (Chen et al. 2014, 2018b) that the down-gradient transport of vorticity should be supplied by attached hairpin-type structures, although we recall the evidence from the previous subsection that D-type vortices are not self-similar at  $Re_{\tau} = 1000$ . An interesting fact that may be inferred from the color plot in Fig 13 is that  $\Sigma_{vz}^{D}$ is not down-gradient (red color) at every point on the D-vortices. In fact, there are points also of very large up-gradient transport (blue color), which is permitted because the filter function  $\mathcal{D}^c$  selects positive flux only in Fourier space not in physical space. We can see furthermore that the regions of the two different signs of transport are organized, with red (down-gradient) generally on the upstream side of the vortex and blue (up-gradient) generally on the downstream side. This tendency is even more obvious in an interactive 3D version of figure 13 that can be found at http://cocalc.com/.../D-vortices.html made available in the JFM Notebook. This observation can be easily understood in terms of the direction of the Lamb vector calculated from the vorticity vector and the local vortex-induced velocity in the vicinity of a hairpin-type vortex.

The net vorticity flux of all D-type eddies is indeed down-gradient, however, as illustrated by Fig 14a which plots  $\langle \Sigma_{yz}^D \rangle$  normalized by  $-u_\tau^2/H$  versus y. Not only is the normalized flux positive but in fact  $\langle \Sigma_{yz}^D \rangle < -u_\tau^2/H$  for all y and it approaches almost  $-7u_\tau^2/H$  in the buffer layer. These large values are possible because they (plus the viscous flux) are nearly cancelled by the opposing up-gradient flux supplied by the complementary field  $\mathbf{u}^U$ . In addition to the total  $\langle \Sigma_{yz}^D \rangle$ , we can also calculate the partial average  $\langle \Sigma_{yz}^D \rangle_{\beta}$  from the region of the vortex cores characterized by  $\lambda_2^D < -\beta \lambda_2^{D,rms}$ . For  $\beta=1$  this may be considered the direct contribution of the D-type vortices to the mean down-gradient flux. However, it is likely that this partial average on the cores underestimates the true contribution of the coherent vortices, which will also make an indirect contribution from a spatial neighborhood influenced by induced motions from Biot-Savart (Wu & Christensen 2006; Chen *et al.* 2018*b*). As a crude estimate



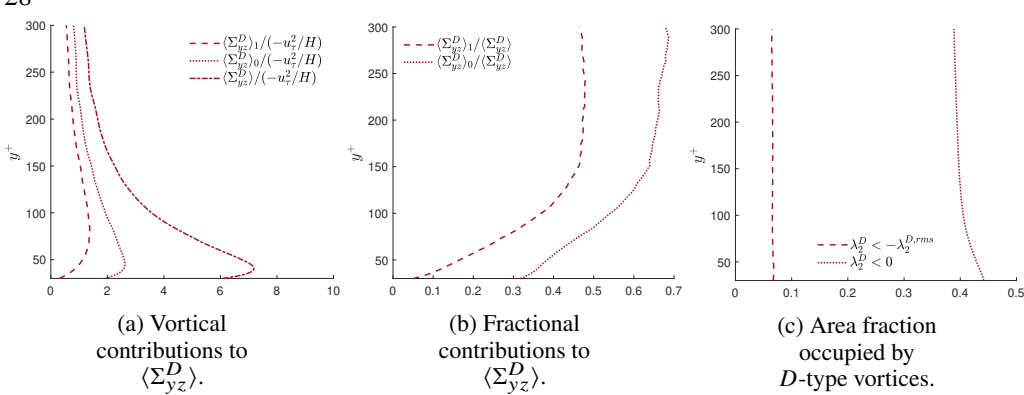


Figure 14: (a) Mean down-gradient vorticity flux and its contributions from *D*-type coherent vortices. (b) Fractional contributions from *D*-type vortices. (c) Area fraction occupied by *D*-type vortices.

of this larger contribution from the region influenced by the coherent vortices, we consider the partial average  $\langle \Sigma_{yz}^D \rangle_0$  over the region with  $\lambda_2^D < 0$ . Both of these partial averages are plotted also versus y in Fig 14a. The fractional contributions of the vortex cores and the vortex neighborhoods are furthermore plotted in Fig. 14b. We can also calculate the area fractions of these two regions in the wall-parallel planes at each distance y and these are plotted in Fig. 14c. These plots show that the vortex cores contribute an increasing fraction of the down-gradient flux for increasing y, starting from  $\sim 5\%$  at  $y^+ = 30$ , reaching  $\sim 45\%$  at  $y^+ = 150$ , and remaining roughly constant then in the log layer, but vortex cores occupy only about  $\sim 7\%$  of the area at every wall distance. The flux fraction from the vortex-dominated region behaves similarly but is even larger, with  $\sim 30\%$  contribution at  $y^+ = 30$ ,  $\sim 65\%$  at  $y^+ = 150$ , and remaining roughly constant thereafter, while occupying only about 40% of the area. Thus, by either of the measures, the D-type vortices make a contribution to the down-gradient flux out of proportion to their volume in the flow.

Our results closely mirror previous works which have studied the effects of coherent vortices on the transport of spanwise vorticity. Following the pioneering work of Wu & Christensen (2006) on spanwise vortex contributions to Reynolds stress, Chen *et al.* (2014) experimentally studied open channel flume flows at  $Re_{\tau} = 382 \sim 740$  using particle image velocimetry (PIV) in 2D vertical planes, which gave access to the velocities u(x, y) and v(x, y). Identifying coherent vortices by the swirling strength with  $\beta = 1.5$ , they could then analyze their contribution to the advective flux  $v\omega_z$ . They found many such coherent vortices with almost 97% prograde at  $y^+ \simeq 50$  and this percentage declining with y but still 65% at  $y^+ = 600$ , and it was conjectured that the prograde vortices were the heads of hairpin vortices. Chen *et al.* (2014) observed as well a bipolar distribution of flux near the vortex cores, with  $v'\omega_z' > 0$  upstream and  $v'\omega_z' < 0$  downstream, which they explained also by local induced velocities. Finally, Chen *et al.* (2014) found for the region  $100 < y^+ < 0.9Re_{\tau}$  that coherent vortex cores contribute about 45% to  $\langle v\omega_z \rangle$  while occupying only 9% of the area. All of these results for the total velocity field in 2D planes are quite similar to ours for the high-pass filtered field component  $\mathbf{u}^D$  in 3D.

The following paper of Chen *et al.* (2018*b*) (see also Chen *et al.* (2018*a*)) verified the results of Chen *et al.* (2014), but in the channel-flow simulation of Del Alamo *et al.* (2004) at  $Re_{\tau} = 934$ . Because of the availability of full 3D velocity fields, Chen *et al.* (2018*b*) could apply the swirling strength criterion for various choices of  $\beta$  in both 2D planes and in 3D and they found that comparable results were obtained for both, although the 3D

criterion identified more coherent vortices than did the 2D criterion. Chen et al. (2018b) could also study the stretching flux  $-w\omega_y$  and the full nonlinear flux  $v\omega_z - w\omega_y$  and then investigate the coherent vortex contribution to each of these. In fact, Chen et al. (2018b) decomposed the entire space domain into four exclusive point sets consisting of "filamentary vortices" (FV), "non-filamentary vortices" (NFV), "non-swirling vortex structures" (NSVS), and "irrotational structures" (IS), and all of these except the latter can contribute to vorticity flux. The FV structures correspond to roughly to our vortex cores, but identified by swirling strength and a region growing algorithm, and the other structure types are precisely defined by Chen et al. (2018a,b). Thus, Chen et al. (2018b) determined the fractional contributions of each of the first three types of structures (FV, NFV, NSVS) to the three fluxes (advective, stretching, total nonlinear) and they emphasized the dominant role of the FV structures. For the region  $y^+ > 300$  of their simulation where  $\langle w\omega_y \rangle > 0$  (down-gradient), FV structures contribute more than 80% while occupying only 15% of the volume. Likewise, for the region  $y^+ > 50$  where  $\langle v\omega_z - w\omega_y \rangle < 0$  (down-gradient), FV structures contribute more than 60% while occupying area less than 15%. They concluded that: "Compared with the other three structures, FV play a very important role in velocity-vorticity correlations and the net force."

From our perspective, however, a very important result of Chen et al. (2018b) that was never explicitly mentioned by them is the fact that the FV contributions to all three of the fluxes are negative (down-gradient) everywhere, that is,  $\langle v\omega_z \rangle_{FV} < 0$ ,  $-\langle w\omega_z \rangle_{FV} < 0$  and  $\langle v\omega_z - w\omega_z \rangle_{FV} < 0$  for all y. These signs can be inferred from the data plotted in Fig. 2(b) and Fig. 9 of Chen et al. (2018b). Since however  $-\langle w\omega_y \rangle > 0$  for  $y^+ < 300$  and  $\langle v\omega_z - w\omega_y \rangle > 0$ for  $y^+ < 50$  in the simulation studied by Chen et al. (2018b), this means that the FV structures are not only not dominant in these regions but in fact give a contribution of the wrong sign! See Fig. 9(c)-(d) in Chen et al. (2018b). Put another way, the FV structures do not account for the up-gradient vorticity transport in these regions. This is understandable if one can essentially identify the FV structures of Chen et al. (2018b) with our D-type vortices, which contribute always a net down-gradient flux. This identification is plausible based on the evidence of visualizations, since the D-type vortices shown in our Fig. 13 resemble quite closely the vortex structures detected by the swirling strength criterion in the full velocity field (Adrian & Liu 2002; Alfonsi et al. 2011). In any case, the important result of Chen et al. (2018b) not emphasized by them is that it is the NFV and NSVS structures which account for the up-gradient vorticity transport observed closer to the wall. Unfortunately, the works of Chen et al. (2018a,b) did not attempt to visualize the NFV and NSVS structures or to clarify their morphology and dynamics.

We can now illuminate the nature of such structures by vortex visualizations for the lowpass field  $\mathbf{u}^U$ , using the discriminant function  $\lambda_2^U$  and  $\beta = 1$ . These structures are plotted in Fig 15 and shall be referred to here as "U-type vortices" since they arise from the field  $\mathbf{u}^U$  which accounts for the up-gradient nonlinear vorticity flux toward the wall. As before, we visualize only the vortices in the log-layer of our simulation and the vortex surfaces are colored based on the values of the up-gradient flux  $\Sigma_{vz}^U$ . The *U*-type vortices visualized in Fig 15 have a pancake structure, vertically flattened and elongated along the streamwise direction but especially along the spanwise direction. Their characteristic shape becomes even clearer in the interactive 3D version of Fig. 15 available at http://cocalc.com/../Uvortices.html. These are exactly the type of vortex structures one would imagine to arise from the Lighthill (1963) mechanism of correlated downflow and lateral stretching. In fact, the roughly twice longer extents spanwise than streamwise correspond well to Lighthill's remark that "some longitudinal deformation is usually also present, which reduces the need for lateral deformation (perhaps, on average, by half)." Note, that these structures, ultimately based on the 2D co-spectra plotted in Fig. 11, can be interpreted as evidence for a cascade process similar to momentum, since these structures are responsible for transfer in scale

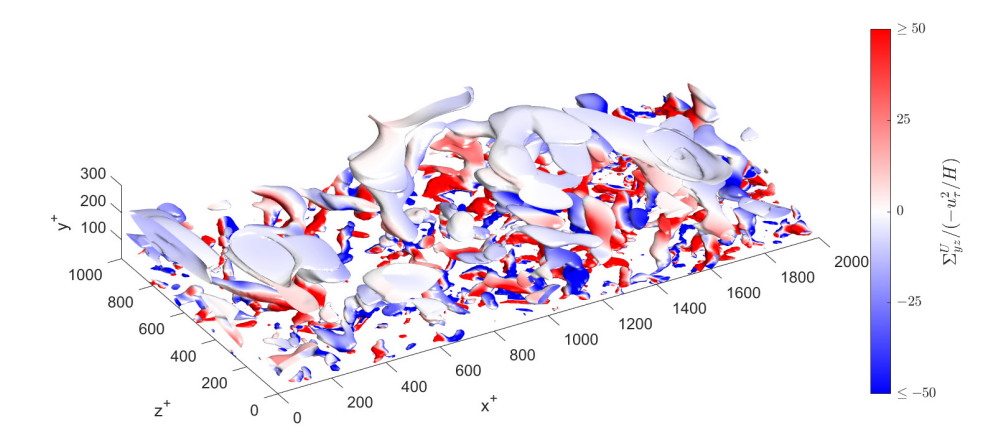


Figure 15: Vortices identified using the  $\lambda_2$ -criterion for the velocity field  $\mathbf{u}^U$  filtered using  $\mathcal{D}$ . Isosurfaces are plotted for  $\lambda_2^U = -\lambda_2^{U,rms}$  and coloured by the nonlinear flux  $\Sigma_{yz}^U$ . The three dimensional figure is available at http://cocalc.com/.../U-vortices.html. The data and code to generate 3D vortices are available at http://cocalc.com/.../3D-vortices/.

and in space. However, there is no obvious self-similarity of these structures in scale and, according to the results presented in our Fig. 8 and Table 2, one might expect the ratio  $\lambda_x/\lambda_z$  to increase with scale. The *U*-type vortices show also no obvious attachment to the wall, being mainly horizontal to it. Indeed, an extension of the AEM by Perry & Marusic (1995); Marusic & Perry (1995) introduced in addition to the "Type-A" attached eddies also "Type-B" eddies to represent the wake flow in the outer layer and small-scale "Type C" eddies to represent the Kolmogorov range. The Type-B eddies were viewed as detached vortex tubes which undulate in the spanwise direction, thus somewhat resembling our Utype eddies (see Figure 3 of Perry & Marusic (1995)). More recently, Hu et al. (2020) have attempted to decompose turbulent channel flow fields at  $Re_{\tau}$  = 5200 into small-scale eddies, attached eddies, and detached eddies, and their |u|-isosurfaces for the detached eddies (see their Fig. 19(d)) have a similar pancake structure as our *U*-type vortices. We have also checked that the vorticity in the *U*-type vortices is predominantly spanwise and prograde consistent with lateral stretching of pre-existing vorticity. This is demonstrated by Fig. G.14 in the Supplementary Materials, where we colour these vortices by the cosine of the angle made by the vorticity vector  $\omega^U$  with the z-axis and find the prevalence of values close to -1, denoting prograde spanwise aligned vortices. Finally, we observe flux-bipolarity of the U-type vortices just as for the D-type, with red (down-gradient) generally on the upstream side of the vortex and blue (up-gradient) generally on the downstream side. This tendency is again more obvious in a 3D version of the figure available in the JFM Notebook.

Despite large contributions to the vorticity flux of both signs, however, the net flux supplied by all U-type eddies is up-gradient. This is verified by the data in Fig 16a which plots  $\langle \Sigma_{yz}^U \rangle$  normalized by  $-u_\tau^2/H$  versus y. Similar to the result for the D-type vortices,  $\langle \Sigma_{yz}^U \rangle \gtrsim u_\tau^2/H$  across most of the log layer and approaches  $10u_\tau^2/H$  at the lower y range where it must cancel most of the down-gradient flux from the D-type eddies and viscous diffusion. For the largest  $y^+ \sim 300$  in the log layer,  $\langle \Sigma_{yz}^U \rangle \simeq 0.1u_\tau^2/H$  and still cancels part of the contribution from the D-type eddies. In addition to the total  $\langle \Sigma_{yz}^U \rangle$ , we can also calculate the partial averages  $\langle \Sigma_{yz}^U \rangle_\beta$  for the condition  $\lambda_2^U < -\beta \lambda_2^{U,rms}$  with  $\beta=1$  (vortex cores) and  $\beta=0$  (vortex neighborhoods). Both of these partial averages are plotted also versus y in Fig 16a,

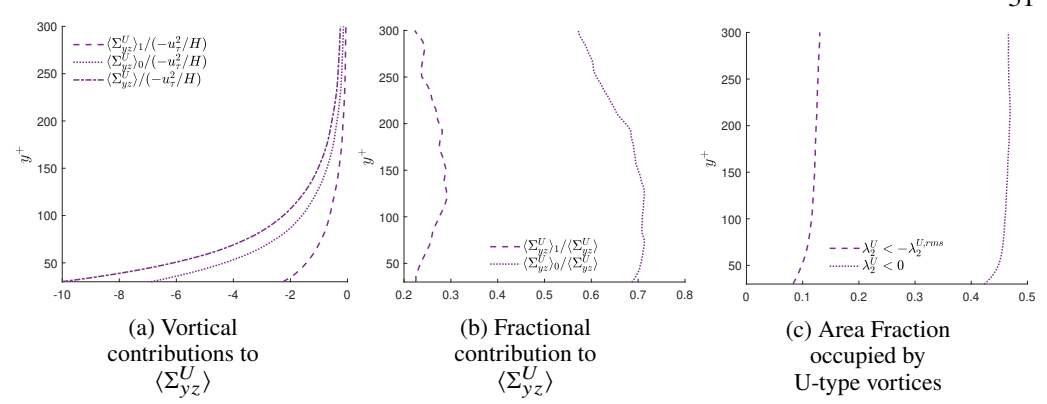


Figure 16: (a) Mean down-gradient vorticity flux and its contributions from U-type coherent vortices. (b) Fractional contributions from U-type vortices. (c) Area fraction occupied by U-type vortices.

the fractional contributions of the vortex cores and the vortex neighborhoods are plotted in Fig. 16b, and the corresponding area fractions plotted in Fig. 16c. We observe that the cores of the U-type vortices account for  $\sim 20\% - 30\%$  of the up-gradient flux but occupy only about 10% of the area, while regions dominated by the U-type vortices provide  $\sim 60\% - 70\%$  of the flux but occupy only about 45% of the area. The coherent U-type vortices thus contribute a percentage of the up-gradient flux roughly twice their area in the flow. This is not as outsize as the contribution of the D-type vortices to the down-gradient flux and the lower performance may be due to our rote application of the  $\lambda_2$ -criterion for vortex identification in  $\mathbf{u}^U$ . This criterion was designed by Jeong & Hussain (1995) to detect rapidly swirling vortex tubes with low-pressure cores, whereas the U-type vortices clearly have a distinct structure. It is also possible that our filter function  $\mathcal D$  does not have spectral support optimally chosen. More appropriate filter kernels and discriminant functions can probably be devised to characterize better the coherent U-type vortices that contribute most to the up-gradient vorticity transport.

## 4. Discussion and Conclusions

The main objective of this work has been to elucidate the dynamics involved in turbulent tranport of spanwise vorticity normal to a solid wall, motivated by the direct connection of this vorticity flux to turbulent drag. We have carried out a numerical study for a canonical case of pressure-driven Poiseuille flow in a channel with plane-parallel walls. We find that the mean vorticity transfer is the result of two intensely competing processes: an up-gradient transfer that concentrates spanwise vorticity strongly near the wall and a slightly greater down-gradient transfer that disposes of the fresh spanwise vorticity generated at the wall by the mean pressure-gradient. This is exactly the picture suggested by Lighthill (1963), who proposed also a concrete mechanism for up-gradient transport by correlated inflow to the wall and lateral stretching of vortex lines as well as outflow correlated with lateral relaxation. We have presented here detailed evidence for the validity of Lighthill's mechanism in the case of turbulent channel flow based upon: (i) correlations of wall-normal velocity with flux of spanwise vorticity, (ii) velocity-vorticity co-spectra that identify the eddies involved in nonlinear vorticity transport in the two directions, and (iii) visualization of the coherent vortex structures which contribute dominantly to the transport. All of the observations that we have accumulated are consistent with the proposed mechanism. In addition, we have provided evidence to support the interpretation of this vorticity flux as a cascade similar to momentum cascade, in that the spatial transport of vorticity is associated also with a transfer

in scale. This verification has consequences that extend far beyond channel flow, because Lighthill (1963) suggested that the up-gradient transfer mechanism has very general validity for all turbulent flows interacting with solid walls, e.g. high-Reynolds flows around bluff bodies or airplane wings. In fact, Lighthill (1963) proposed this mechanism to explain why turbulent boundary layers with concentrated vorticity form generally near solid walls. This is the necessary prelude to another fundamental vortex interaction with solid walls, the violent eruption of vorticity away from the wall (Doligalski *et al.* 1994; Smith *et al.* 1991), which apparently underlies phenomena such as boundary-layer separation behind bluff bodies and frequent ejections from the walls in turbulent flows over flat plates and in straight pipes.

Our work exposes also a limitation of the "attached eddy model" of Townsend (1976) because we find considerable evidence that down-gradient vorticity flux out from solid walls is provided indeed by attached eddies but that the competing up-gradient flux into the walls is carried by detached eddies. Of course, many extensions of the AEM have been proposed previously. We have already mentioned the early work of Perry & Marusic (1995); Marusic & Perry (1995) and see also more recent papers of Chandran et al. (2020); Hu et al. (2020). The spectral aspects of the extension by Perry & Marusic (1995); Marusic & Perry (1995) focus on the streamwise spectrum  $\phi_{uu}(k_x)$ , as summarised in Figure 16 of Marusic & Perry (1995), reproduced in Figure 11 of Marusic & Monty (2019). Our present cospectral results echo features of this model upon suitable interpretation. The model of Perry & Marusic (1995); Marusic & Perry (1995) has an overlap in the streamwise scales of Type-A and Type-B eddies, with the latter contribution dominating at larger streamwise scales. This type of behaviour is seen also in our 2D flux co-spectra in the log layer, plotted in Fig 11 (d),(e),(f), where the U-type eddies dominate at large streamwise scales but overlap with the support of the D-type eddies at smaller streamwise scales. Note, however, that the effect of Type-B eddies in the AEM extension of Perry & Marusic are supposed to diminish upon approaching the wall, whereas the vorticity transport effects of the U-type eddies in our work increase and dominate close to the wall. Unlike previous proposals to extend the AEM, our work has revealed that detached eddies play a fundamental dynamical role in the near-wall region, with direct importance to drag generation and reduction. The closest connection of our results are with those of Chen et al. (2018b), who found that "non-filamentary vortices" (NFV) and "non-swirling vorticity structures" (NSVS) rather than "filamentary vortices" (FV) are responsible for the dominant up-gradient nonlinear vorticity transport near the wall.

In this paper we have exploited a database of a turbulent channel flow at  $Re_{\tau}=1000$  and we have compared with related experiments and simulations at comparable Reynolds numbers. However, empirical data is available at a broader range of Reynolds numbers, both lower-Reynolds simulation data (Bernard 1990; Crawford & Karniadakis 1997) and field experiments at much higher Reynolds numbers (Priyadarshana *et al.* 2007; Morrill-Winter & Klewicki 2013). We do not expect the main conclusions of our work to be *Re*-dependent and we are aware of no data available at other Reynolds numbers which contradicts them. However, some details of the story we have presented may change with Re. For example, it is well-known that many predictions of the AEM are observable only for  $Re \gg 1$  and, in particular, Chandran *et al.* (2017) estimate that the similarity relation  $\lambda_z \sim \lambda_x$  for attached eddies and clear  $k^{-1}$  energy spectra for both  $k_x$  and  $k_z$  should be observable only for  $Re_{\tau} > 60,000$ . Thus, our conclusion in section 3.3 that *D*-type and *U*-type eddies are non-self-similar might be Reynolds-number dependent, especially since self-similarity for 2D energy cospectra that is expected from attached eddies is not observed either at comparable  $Re_{\tau}$  (Del Alamo *et al.* 2004; Chandran *et al.* 2017). Thus, extending our analysis to higher Reynolds numbers is an important direction for future research.

Another important direction is the investigation of turbulent vorticity dynamics by means of stochastic Lagrangian methods (Constantin & Iyer 2011; Eyink *et al.* 2020*a*). The heuristic

arguments of Lighthill (1963) are essentially Lagrangian and invoke the remarkable "frozenin" properties enjoyed by vortex-lines in smooth ideal Euler flows. In a physical turbulent flow, however, these familiar properties of ideal vortex-lines suffer fundamental modifications by viscous diffusion, which can be exactly captured by the stochastic Lagrangian representation of vortex dynamics. These methods have already proved powerful to verify the validity of Lighthill's argument for origin of large magnitudes of wall-vorticity in a transitional zero pressure-gradient boundary layer (Wang et al. 2022). The advantage of these methods compared with the Eulerian analysis in the present work is that they provide a complete and unambiguous account of the origin of the vorticity at any point in the flow, with precise and quantitative information about the physical mechanisms involved. Such stochastic Lagrangian methods have already been applied to "ejections" and "sweeps" in the buffer layer of the same  $Re_{\tau} = 1000$  turbulent channel flow studied in this paper, where it was demonstrated that the spanwise vorticity in those events is not assembled abruptly from wall-vorticity but instead over many hundreds of viscous times (Eyink et al. 2020b). It would be very illuminating to apply these methods in the log layer of the channel flow, reconstructing the spanwise vorticity under conditions of inflow and outflow and determining its origin unambiguously. The existing numerical schemes for the stochastic Lagrangian approach are quite inefficient in the log layer, however, because the Monte Carlo sampling errors grow exponentially in time. New algorithmic approaches are probably therefore required.

Finally, the insights that we have obtained in this work about Eulerian vorticity dynamics described by the Huggins vorticity flux tensor (1.4) can be exploited to understand drag generation and reduction via the detailed Josephson-Anderson (JA) relation (Huggins 1970, 1994; Eyink 2008, 2021). Such work is already in progress (Kumar & Eyink 2023). We have thus intentionally omitted in the present paper any discussion of the work of Yoon et al. (2016) which directly relates velocity-vorticity correlations to mean drag by a version of the so-called FIK identity (Fukagata et al. 2002). This discussion requires a careful comparison with the JA-relation, which will be done by Kumar & Eyink (2023). The connections between these two approaches is indeed not straightforward, e.g. down-gradient nonlinear vorticity flux produces drag in the JA-relation but reduces drag in the identity of Yoon et al. (2016)! Here we just mention the principal difference that, whereas the identity of Yoon et al. (2016) represents the mean drag in a Reynolds averaging approach, the JA-relation connects the drag *instantaneously* in time to the vorticity flux throughout the flow volume. The shift away from ensemble flow statistics to recognize the dynamical heterogeneity and intermittency of drag has proved important, for example, in the problem of polymer drag reduction (Xi 2019). Our results here shed new light on the latter problem, because they imply that drag can be reduced instantaneously either by decreasing the down-gradient flux of spanwise vorticity or by increasing the up-gradient flux, or both. This will also be the subject of future work.

**Acknowledgements.** We thank Professors Nigel Goldenfeld, Bjorn Hof, Yves Pomeau and Tamer Zaki for fruitful discussions and the JHTDB team for their help and support of the public numerical turbulence laboratory.

**Funding:** We thank also the Simons Foundation for support of this work through the Targeted Grant No. MPS-663054, "Revisiting the Turbulence Problem Using Statistical Mechanics", and the National Science Foundation (Grant # CSSI-210387) for support of JHTDB and of pursuing analysis of wall-bounded turbulence.

**Declaration of interests.** The authors report no conflict of interest.

**Author ORCIDs.** 

- S. Kumar https://orcid.org/0000-0002-6785-0072.
- C. Meneveau https://orcid.org/0000-0001-6947-3605.
- G. Eyink https://orcid.org/0000-0002-8656-7512.

#### REFERENCES

- ADRIAN, R. J. 2007 Hairpin vortex organization in wall turbulence. *Physics of fluids* 19 (4), 041301.
- Adrian, R. J. & Liu, Z. 2002 Observation of vortex packets in direct numerical simulation of fully turbulent channel flow. *Journal of Visualization* **5** (1), 9–19.
- Alfonsi, G., Ciliberti, S. A., Mancini, M. & Primavera, L. 2011 Hairpin vortices in turbulent channel flow. *Procedia Computer Science* **4**, 801–810.
- Anderson, P. W. 1966 Considerations on the flow of superfluid helium. Rev. Mod. Phys. 38, 298–310.
- AROSEMENA, A. A. & SOLSVIK, J. 2022 Velocity–vorticity correlations and the four-layer regime in turbulent channel flow of generalized newtonian fluids. *European Journal of Mechanics B/Fluids* **91**, 1–8.
- BALAKUMAR, B. J. & ADRIAN, R. J. 2007 Large- and very-large-scale motions in channel and boundary-layer flows. *Philosophical Transactions of the Royal Society A: Mathematical, Physical and Engineering Sciences* **365** (1852), 665–681, arXiv: https://royalsocietypublishing.org/doi/pdf/10.1098/rsta.2006.1940.
- Bernard, P. S. 1990 Turbulent vorticity transport in three dimensions. *Theoretical and Computational Fluid Dynamics* **2** (3), 165–183.
- BOGARD, D. G. & TIEDERMAN, W. G. 1986 Burst detection with single-point velocity measurements. *Journal of Fluid Mechanics* **162**, 389–413.
- Brown, G. L., Lee, M. & Moser, R. D. 2015 Vorticity transport: the transfer of viscous stress to Reynolds stress in turbulent channel flow. In *Ninth International Symposium on Turbulence and Shear Flow Phenomena (TSFP-9)*, vol. 2, talk 6B-5. Begel House Inc.
- Cantwell, B. J. 1981 Organized motion in turbulent flow. Annual review of fluid mechanics 13 (1), 457-515.
- Chakraborty, P., Balachandar, S. & Adrian, R. J. 2005 On the relationships between local vortex identification schemes. *Journal of fluid mechanics* **535**, 189–214.
- Chandran, D., Baidya, R., Monty, J. P. & Marusic, I. 2017 Two-dimensional energy spectra in high-Reynolds-number turbulent boundary layers. *Journal of Fluid Mechanics* 826.
- Chandran, D., Monty, J. P. & Marusic, I. 2020 Spectral-scaling-based extension to the attached eddy model of wall turbulence. *Physical Review Fluids* 5 (10), 104606.
- Chen, H., Li, D., Bai, R. & Wang, X. 2018a Comparison of swirling strengths derived from two-and three-dimensional velocity fields in channel flow. *AIP Advances* 8 (5), 055302.
- CHEN, H., LI, D., BAI, R. & WANG, X. 2018b Contributions of vortical/non-vortical structures to velocity–vorticity correlations and net force in channel flow. *Journal of the Physical Society of Japan* 87 (9), 094402.
- Chen, Q., Adrian, R. J., Zhong, Q., Li, D. & Wang, X. 2014 Experimental study on the role of spanwise vorticity and vortex filaments in the outer region of open-channel flow. *Journal of Hydraulic Research* **52** (4), 476–489.
- CHIN, C., PHILIP, J., KLEWICKI, J. C., OOI, A. & MARUSIC, I. 2014 Reynolds-number-dependent turbulent inertia and onset of log region in pipe flows. *Journal of Fluid Mechanics* **757**, 747–769.
- Constantin, P. & Iyer, G. 2011 A stochastic-lagrangian approach to the Navier–Stokes equations in domains with boundary. *The Annals of Applied Probability* **21** (4), 1466–1492.
- Crawford, C. H. & Karniadakis, G. E. 1997 Reynolds stress analysis of emhd-controlled wall turbulence. part i. streamwise forcing. *Physics of Fluids* **9** (3), 788–806.
- Del Alamo, J. C., Jiménez, J., Zandonade, P. & Moser, R. D. 2004 Scaling of the energy spectra of turbulent channels. *Journal of Fluid Mechanics* **500**, 135–144.
- Doligalski, T. L., Smith, C. R. & Walker, J. D. A. 1994 Vortex interactions with walls. *Annual Review of Fluid Mechanics* **26** (1), 573–616.
- EYINK, G. L. 2008 Turbulent flow in pipes and channels as cross-stream "inverse cascades" of vorticity. *Physics of Fluids* **20** (12), 125101.
- EYINK, G. L. 2021 Josephson-anderson relation and the classical d'alembert paradox. *Phys. Rev. X* 11, 031054.
- EYINK, G. L., GUPTA, A. & ZAKI, T. A 2020a Stochastic lagrangian dynamics of vorticity. Part 1. General theory for viscous, incompressible fluids. *Journal of Fluid Mechanics* **901**.

- EYINK, G. L., GUPTA, A. & ZAKI, T. A. 2020b Stochastic Lagrangian dynamics of vorticity. Part 2. Application to near-wall channel-flow turbulence. *Journal of Fluid Mechanics* 901.
- Fukagata, K., Iwamoto, K. & Kasagi, N. 2002 Contribution of Reynolds stress distribution to the skin friction in wall-bounded flows. *Physics of Fluids* **14** (11), L73–L76.
- Graham, J., Kanov, K., Yang, X. I. A., Lee, M., Malaya, N., Lalescu, C. C., Burns, R., Eyink, G., Szalay, A., Moser, R. D. & Meneveau, C. 2016 A web services accessible database of turbulent channel flow and its use for testing a new integral wall model for les. *Journal of Turbulence* 17 (2), 181–215.
- Graham, M. D. & Floryan, D. 2021 Exact coherent states and the nonlinear dynamics of wall-bounded turbulent flows. *Annual Review of Fluid Mechanics* **53**, 227–253.
- Guala, M., Hommema, S. E. & Adrian, R. J. 2006 Large-scale and very-large-scale motions in turbulent pipe flow. *Journal of Fluid Mechanics* **554**, 521–542.
- HALLER, G., HADJIGHASEM, A., FARAZMAND, M. & HUHN, F. 2016 Defining coherent vortices objectively from the vorticity. *Journal of Fluid Mechanics* **795**, 136–173.
- Hu, R., Yang, X. I. A. & Zheng, X. 2020 Wall-attached and wall-detached eddies in wall-bounded turbulent flows. *Journal of Fluid Mechanics* 885, A30.
- Huggins, E. R. 1970 Energy-dissipation theorem and detailed Josephson equation for ideal incompressible fluids. *Phys. Rev. A* **1**, 332–337.
- Huggins, E. R. 1994 Vortex currents in turbulent superfluid and classical fluid channel flow, the Magnus effect, and Goldstone boson fields. *Journal of Low Temperature Physics* **96** (5), 317–346.
- Hunt, J. C. R., Wray, A. A. & Moin, P. 1988 Eddies, streams, and convergence zones in turbulent flows. In *Studying turbulence using numerical simulation databases*, 2. *Proceedings of the 1988 summer program, Center for Turbulence Research*, pp. 193–208. Ames Research Center.
- Hussain, A. K. M. F. 1986 Coherent structures and turbulence. *Journal of Fluid Mechanics* 173, 303–356.
- Hwang, J., Lee, J., Sung, H. J. & Zaki, T. A. 2016 Inner–outer interactions of large-scale structures in turbulent channel flow. *Journal of Fluid Mechanics* **790**, 128–157.
- Hwang, J. & Sung, H. J. 2018 Wall-attached structures of velocity fluctuations in a turbulent boundary layer. *Journal of Fluid Mechanics* **856**, 958–983.
- JEONG, J. & HUSSAIN, A. K. M. F. 1995 On the identification of a vortex. *Journal of Fluid Mechanics* 285, 69–94.
- JEONG, J., HUSSAIN, F., SCHOPPA, W. & KIM, J. 1997 Coherent structures near the wall in a turbulent channel flow. *Journal of Fluid Mechanics* 332, 185–214.
- JIMÉNEZ, J. 2012 Cascades in wall-bounded turbulence. Annual Review of Fluid Mechanics 44, 27-45.
- JOSEPHSON, B. D. 1965 Potential differences in the mixed state of type ii superconductors. *Phys. Lett.*; (Netherlands) 16.
- Kim, K. C. & Adrian, R. J. 1999 Very large-scale motion in the outer layer. *Physics of Fluids* 11 (2), 417–422.
- Klewicki, J. C. 1989 Velocity–vorticity correlations related to the gradients of the reynolds stresses in parallel turbulent wall flows. *Physics of Fluids A: Fluid Dynamics* 1 (7), 1285–1288.
- KLEWICKI, J. C., FIFE, P., WEI, T. & McMurtry, P. 2007 A physical model of the turbulent boundary layer consonant with mean momentum balance structure. *Philo. Trans. Roy. Soc. A* **365** (1852), 823–840.
- KLEWICKI, J. C., MURRAY, J. A. & FALCO, R. E. 1994 Vortical motion contributions to stress transport in turbulent boundary layers. *Physics of Fluids* 6 (1), 277–286.
- Kolář, V. 2007 Vortex identification: New requirements and limitations. *International journal of heat and fluid flow* **28** (4), 638–652.
- Kumar, S. & Eyink, G. L. 2023 Turbulent drag in generalized channel flows and the Josephson-Anderson relation. in preparation.
- LEE, M., MALAYA, N. & MOSER, R. D. 2013 Petascale direct numerical simulation of turbulent channel flow on up to 786k cores. In SC'13: Proceedings of the International Conference on High Performance Computing, Networking, Storage and Analysis, pp. 1–11. IEEE.
- Lee, M. & Moser, R. D. 2015 Direct numerical simulation of turbulent channel flow up to  $Re_{\tau} \approx 5200$ . *Journal of Fluid Mechanics* **774**, 395–415.
- Li, Y., Perlman, E., Wan, M., Yang, Y., Meneveau, C., Burns, R., Chen, S., Szalay, A. & Eyink, G. L. 2008 A public turbulence database cluster and applications to study lagrangian evolution of velocity increments in turbulence. *Journal of Turbulence* 9, N31.
- LIGHTHILL, M. J. 1963 Introduction: Boundary layer theory. In *Laminar Boundary Theory* (ed. L. Rosenhead), pp. 46–113. Oxford: Oxford University Press.

- LOZANO-DURÁN, A., FLORES, O. & JIMÉNEZ, J. 2012 The three-dimensional structure of momentum transfer in turbulent channels. *Journal of Fluid Mechanics* **694**, 100–130.
- Lu, S. S. & Willmarth, W. W. 1973 Measurements of the structure of the reynolds stress in a turbulent boundary layer. *Journal of Fluid Mechanics* **60** (3), 481–511.
- LYMAN, F.A. 1990 Vorticity production at a solid boundary. Appl. Mech. Rev 43 (8), 157–158.
- MARUSIC, I. & MONTY, J. P. 2019 Attached eddy model of wall turbulence. *Annual Review of Fluid Mechanics* **51**, 49–74.
- MARUSIC, I. & PERRY, A. E. 1995 A wall-wake model for the turbulence structure of boundary layers. part 2. further experimental support. *Journal of Fluid Mechanics* **298**, 389–407.
- McKeon, B. J. 2017 The engine behind (wall) turbulence: perspectives on scale interactions. *Journal of Fluid Mechanics* **817**.
- Meinhart, C. D. & Adrian, R. J. 1995 On the existence of uniform momentum zones in a turbulent boundary layer. *Physics of Fluids* 7 (4), 694–696.
- MEYERS, J. & MENEVEAU, C. 2013 Flow visualization using momentum and energy transport tubes and applications to turbulent flow in wind farms. *Journal of Fluid Mechanics* **715**, 335–358.
- Monty, J. P., Klewicki, J. C. & Ganapathisubramani, B. 2011 Characteristics of momentum sources and sinks in turbulent channel flow. In *Seventh International Symposium on Turbulence and Shear Flow Phenomena*. Begel House Inc.
- MORRILL-WINTER, C. & KLEWICKI, J. C. 2013 Influences of boundary layer scale separation on the vorticity transport contribution to turbulent inertia. *Physics of Fluids* **25** (1), 015108.
- MORTON, B. R. 1984 The generation and decay of vorticity. *Geophysical & Astrophysical Fluid Dynamics* **28** (3-4), 277–308.
- NICKELS, T. B., MARUSIC, I., HAFEZ, S. & CHONG, M. S. 2005 Evidence of the  $k_1^{-1}$  law in a high-Reynolds-number turbulent boundary layer. *Physical review letters* **95** (7), 074501.
- PACKARD, R. E. 1998 The role of the josephson-anderson equation in superfluid helium. *Reviews of Modern Physics* **70** (2), 641.
- Panton, R.L. 1984 Incompressible Flow. John Wiley & Sons.
- Perry, A. E. & Marusic, I. 1995 A wall-wake model for the turbulence structure of boundary layers. part 1. extension of the attached eddy hypothesis. *Journal of Fluid Mechanics* **298**, 361–388.
- POPE, S. B. 2000 Turbulent flows. Cambridge university press.
- PRIYADARSHANA, P. J. A., KLEWICKI, J. C., TREAT, S. & Foss, J. F. 2007 Statistical structure of turbulent-boundary-layer velocity-vorticity products at high and low reynolds numbers. *Journal of Fluid Mechanics* **570**, 307–346.
- ROBINSON, S. K. 1991 Coherent motions in the turbulent boundary layer. *Annual review of fluid mechanics* **23** (1), 601–639.
- SMITH, C. R., WALKER, J. D. A., HAIDARI, A. H. & SOBRUN, U. 1991 On the dynamics of near-wall turbulence. *Philosophical Transactions of the Royal Society of London. Series A: Physical and Engineering Sciences* **336** (1641), 131–175.
- STEVENSON, P. M. 1981 Optimized perturbation theory. Phys. Rev. D 23, 2916–2944.
- TAYLOR, G. I. 1915 Eddy motion in the atmosphere. Philos. Trans. R. Soc. London, Ser. A 215 (1), 1–26.
- Taylor, G. I. 1932 The transport of vorticity and heat through fluids in turbulent motion. *Proceedings of the Royal Society of London. Series A, Containing Papers of a Mathematical and Physical Character* **135** (828), 685–702.
- Tennekes, H. & Lumley, J. L. 1972 A first course in turbulence. MIT press.
- Terrington, S. J., Hourigan, K. & Thompson, M. C. 2021 The generation and diffusion of vorticity in three-dimensional flows: Lyman's flux. *Journal of Fluid Mechanics* 915.
- Terrington, S. J., Hourigan, K. & Thompson, M. C. 2022 Vorticity generation and conservation on generalised interfaces in three-dimensional flows. *Journal of Fluid Mechanics* **936**.
- Townsend, A. A. 1976 The Structure of Turbulent Shear Flow, 2nd edn. Cambridge University Press.
- Varoquaux, E. 2015 Anderson's considerations on the flow of superfluid helium: Some offshoots. *Reviews of Modern Physics* 87 (3), 803.
- VIDAL, A., NAGIB, H. M. & VINUESA, R. 2018 Vorticity fluxes and secondary flow: Relevance for turbulence modeling. *Phys. Rev. Fluids* **3**, 072602.
- Wang, M., Eyink, G. L. & Zaki, T. A. 2022 Origin of enhanced skin friction at the onset of boundary-layer transition. *Journal of Fluid Mechanics* **941**.

- WEI, T., FIFE, P., KLEWICKI, J. C. & McMurtry, P. 2005 Properties of the mean momentum balance in turbulent boundary layer, pipe and channel flows. *Journal of Fluid Mechanics* **522**, 303–327.
- WILLMARTH, W. W. & Lu, S. S. 1972 Structure of the reynolds stress near the wall. *Journal of Fluid Mechanics* **55** (1), 65–92.
- Wu, X., Baltzer, J. R. & Adrian, R. J. 2012 Direct numerical simulation of a 30r long turbulent pipe flow at r = 685: large- and very large-scale motions. *Journal of Fluid Mechanics* **698**, 235–281.
- Wu, X. & Moin, P. 2009 Direct numerical simulation of turbulence in a nominally zero-pressure-gradient flat-plate boundary layer. *Journal of Fluid Mechanics* **630**, 5–41.
- Wu, Y. & Christensen, K. T. 2006 Population trends of spanwise vortices in wall turbulence. *Journal of Fluid Mechanics* 568, 55–76.
- XI, L. 2019 Turbulent drag reduction by polymer additives: Fundamentals and recent advances. *Physics of Fluids* 31 (12), 121302.
- YANG, X. I. A., MARUSIC, I. & MENEVEAU, C. 2016 Moment generating functions and scaling laws in the inertial layer of turbulent wall-bounded flows. *Journal of Fluid Mechanics* **791**.
- Yoon, M., Ahn, J., Hwang, J. & Sung, H. J. 2016 Contribution of velocity-vorticity correlations to the frictional drag in wall-bounded turbulent flows. *Physics of Fluids* **28** (8), 081702.
- ZAKI, T. A. 2013 From streaks to spots and on to turbulence: exploring the dynamics of boundary layer transition. *Flow, turbulence and combustion* **91**, 451–473.

#### SUPPLEMENTARY MATERIALS

### A. Quadrant contributions

Partial averages of the flux terms  $v\omega_z - w\omega_y$ ,  $v\omega_z$  and  $-w\omega_y$  conditioned on "low speed (u' < 0)" and "high speed (u' > 0)" events are shown in Fig A.1a, A.1b and A.1c respectively. The plot in Fig A.1c shows that the stretching/tilting term  $(-w\omega_v)$  is agnostic to the sign of u' for  $y^+ \lesssim 100$ , where both low speed and high speed streaks produce up-gradient contributions. For  $100 \lesssim y^+ \lesssim 500$  low speed streaks make down-gradient contributions while high speed streaks make up-gradient contributions to this stretching term. Close to the centerline ( $y^+ \gtrsim 500$ ), both contributions are down-gradient. The convective term (shown in Fig A.1b), on the other hand, shows strongly opposing behaviours for low speed and high speed streaks across nearly the entire channel (for  $y^+ \lesssim 700$ ), with low speed streaks making down-gradient contributions but high speed streaks up-gradient contributions. By contrast, both contributions to the convective flux are down-gradient close to the centerline  $(y^+ \gtrsim 700)$ . The total nonlinear flux (shown in Fig. A.1a), is dominated by the convective term and behaves similarly across most of the channel (5  $\lesssim y^+ \lesssim 700$ ), with low-speed streaks being down-gradient and high-speed streaks being up-gradient. Within the viscous sublayer( $y^+ \le 5$ ), low speed streaks make no contributions to the flux and the entire flux is due to high speed streaks. Close to the centerline  $(y^+ \gtrsim 700)$  both contributions are downgradient. The observed correlations of the separate flux terms with u' are plausibly explained as a consequence of the primary correlation with v' due to Lighthill's mechanism and the secondary correlation of v' with u'.

This idea is illuminated by the quadrant correlations, discussed next. The contributions from the four individual quadrants of the u'-v' plane (see Pope (2000)) are shown for the total nonlinear flux (Fig A.2a), the convection/advection term (Fig A.2b) and the stretching/tilting term (Fig A.2c). Contributions from "active (Q2+Q4)" and "inactive (Q1 +Q3)" motions are plotted as well. The latter show that active motions contribute nearly the entire flux for the convective term, while inactive motions make a much a smaller contribution (Fig A.2b). The stretching/tilting term is nearly agnostic to active/inactive motions for  $y^+ \leq 30$  but also dominated by active motions for  $y^+ \geq 30$  (Fig A.2c). On the whole, the net nonlinear flux (Fig A.2a) is dominated by contributions from active motions, with inactive motions making a decidedly smaller contribution, and this effect is mainly through the convection term. These observations are consistent with our explanation above that the observed correlations of the flux contributions are due to the primary correlation with v' and the strong anti-correlation between u' and v' in Q2 + Q4

Further evidence for this picture is provided by the separate quadrant contributions. From Fig A.2b for the convective term it may be seen that Q1 and Q2 where v'>0 both make down-gradient contributions, while Q3 and Q4 where v'<0 both make up-gradient contributions across the entire channel. On the other hand, the stretching/tilting term in Fig A.2c exhibits opposite flux directions across most of the channel, with Q1 and Q2 up-gradient and Q3 and Q4 down-gradient. Furthermore, for both convection and stretching terms, the Q1 correlations while similar to the Q2 correlations are smaller in magnitude, and likewise the Q3 correlations while similar to the Q4 correlations are smaller. This suggests again that the primary correlation is with v', but that the dominant contribution arises from the "active" quadrants Q2 + Q4 where u' and v' are anti-correlated.

Altogether, these results support our claim that the correlation most relevant to the physics is that between the flux and regions of outflow (v' > 0) and inflow (v' < 0), as shown in Fig 7 in the main text. The dominance of the "active" regions produces a secondary correlation of vorticity flux with u'.

We note that contributions to vorticity flux from the four quadrants Q1-Q4 were calculated previously by Vidal *et al.* (2018), but for duct flow with sidewalls (both straight and curved) at two constant z planes. We cannot compare our results with theirs, not only because of the differences in the simulated flows but also because they considered products of fluctuating terms  $v'\omega_z'$  and  $w'\omega_y'$ . Since  $w\omega_y = w'\omega_y'$ , our results for this term agree well with theirs for z away from sidewalls, but our results for  $v\omega_z$  differ considerably from theirs for  $v'\omega_z'$ .

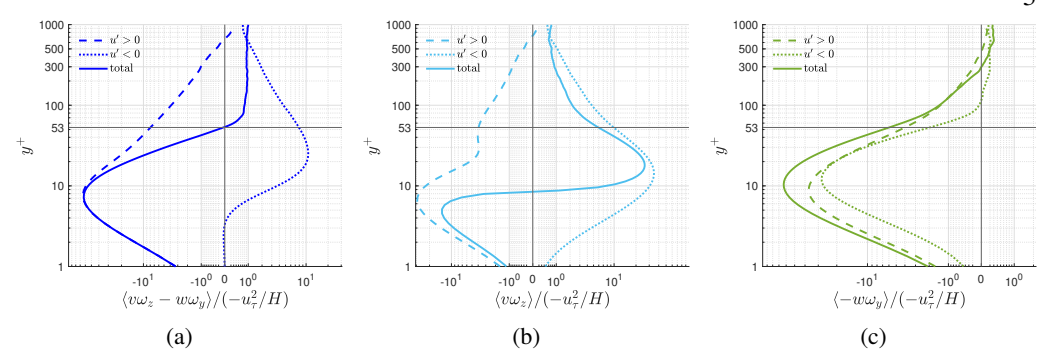


Figure A.1: Contributions from high speed streaks (u' > 0) and low speed streaks (u' < 0), to the (a) nonlinear flux, (b) convection/advection and (c) stretching/tilting, averaged over time and wall parallel planes, plotted as a function of wall distance.

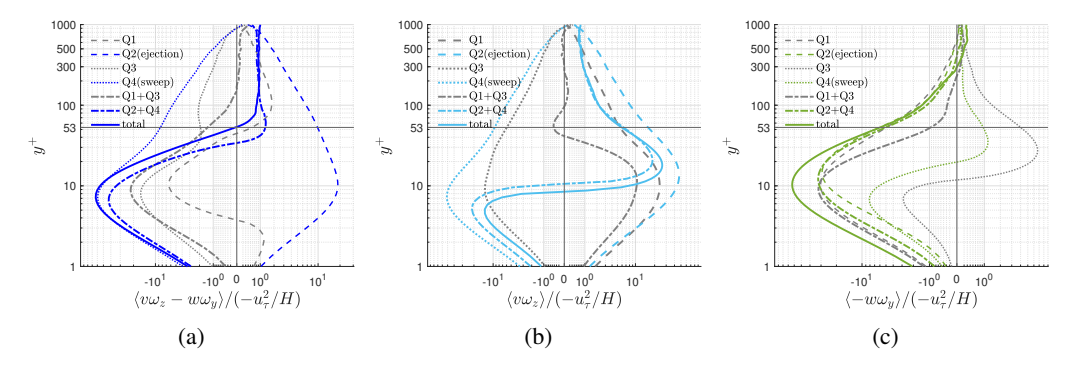


Figure A.2: Contributions from quadrants to the nonlinear flux (a), convection/advection (b) and stretching/tilting (c), averaged over time and wall parallel planes, plotted as a function of wall distance.

# B. Comparison with data from Del Alamo et al. (2004)

We compare the spanwise two point velocity-vorticity correlations computed from channel flow data at  $Re_{\tau} = 1000$  from the Johns Hopkins Turbulence Database Li *et al.* (2008); Graham *et al.* (2016) and at  $Re_{\tau} = 934$  from Del Alamo *et al.* (2004) reported in Monty *et al.* (2011) in Fig B.3. The correlations are related to the respective spanwise co-spectra as follows:

$$R_{w\omega_y}^+(\Delta z) = \frac{R_{w\omega_y}(\Delta z)}{u_\tau^2/\delta_y} = \frac{1}{u_\tau^2/\delta_y} \int_0^\infty \phi_{w\omega_y}(k_z) e^{ik_z \Delta z} dk_z$$
 (B.1)

$$R_{\nu\omega_z}^+(\Delta z) = \frac{R_{\nu\omega_z}(\Delta z)}{u_\tau^2/\delta_\nu} = \frac{1}{u_\tau^2/\delta_\nu} \int_0^\infty \phi_{\nu\omega_z}(k_z) e^{ik_z\Delta z} dk_z$$
 (B.2)

We observe good agreement between correlations from both datasets.

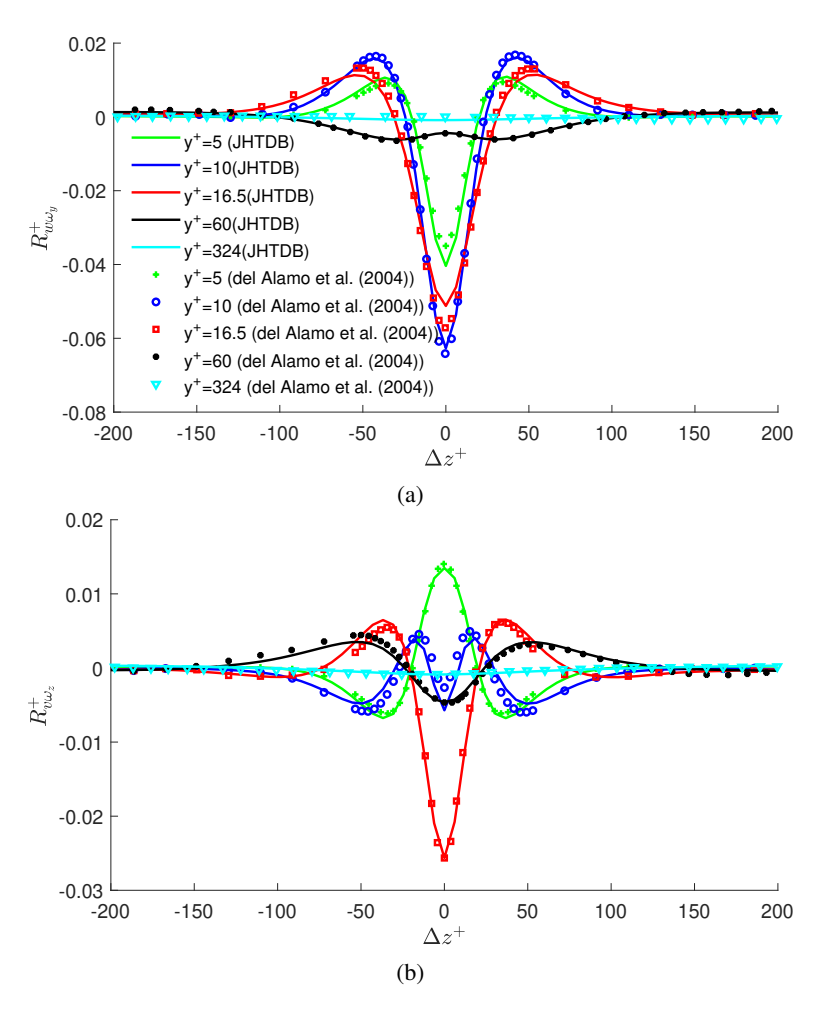


Figure B.3: Spanwise two-point correlation of (a) spanwise velocity and wall normal vorticity ( $R_{w\omega_y}^+$ ), (b) spanwise vorticity and wall normal velocity ( $R_{w\omega_z}^+$ ), computed from channel flow data at  $Re_{\tau}=1000$  from JHTDB( Graham *et al.* (2016)) and from earlier simulation data of channel flow at  $Re_{\tau}=934$  by Del Alamo *et al.* (2004) reported in Monty *et al.* (2011).

# C. Velocity-vorticity co-spectra

The co-spectrum of nonlinear flux is given by  $\phi_{v\omega_z} - \phi_{w\omega_y}$  with the spanwise co-spectra shown in Fig. 8 and the streamwise cospectrum in Fig. 10 of the main text. In this section, we look at the constituent co-spectra, i.e.,  $\phi_{v\omega_z}$  and  $-\phi_{w\omega_y}$ , both spanwise and streamwise. All of the mean features of these 1D spectra can be inferred from the corresponding 2D cospectra plotted in Section E. However, we present the 1D cospectra here for completeness.



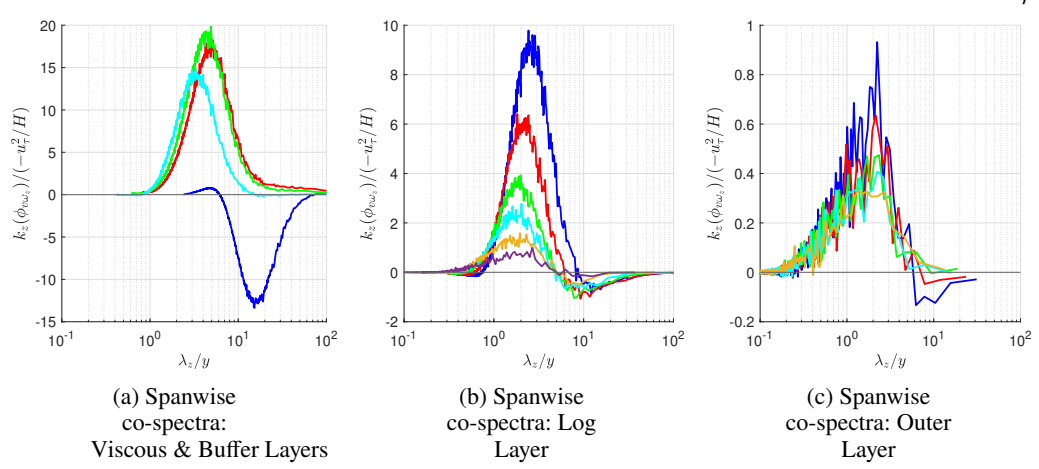


Figure C.4: Normalized spanwise cospectra of wall normal velocity- spanwise vorticity  $(\phi_{V}\omega_z)$ , in the (a) viscous & buffer layers, (b) log layer and (c) outer layer. Curves have the same meaning as in corresponding plots in Fig 8.

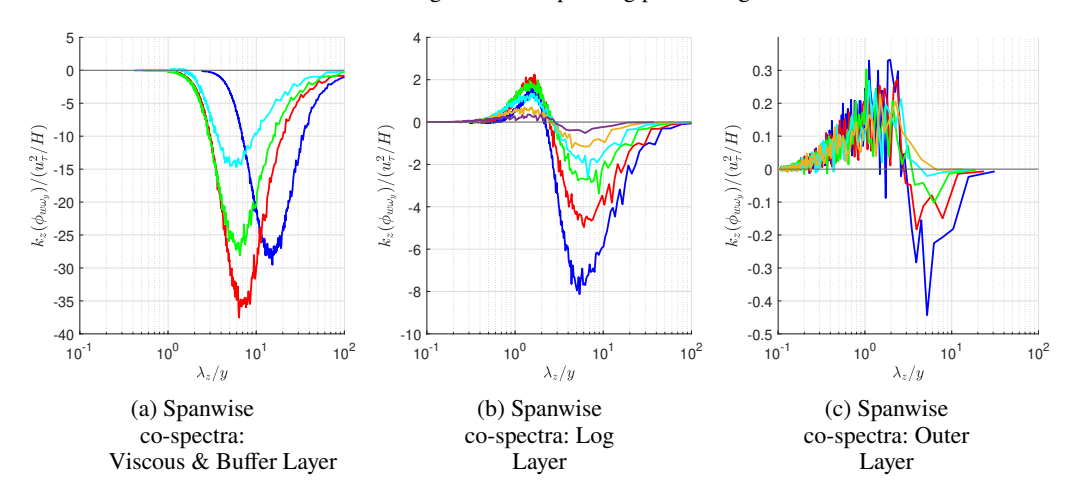


Figure C.5: Normalized spanwise cospectra of (negative of) the spanwise velocity - wall normal vorticity  $(-\phi_W \omega_y)$ , in the (a) viscous & buffer layers, (b) log layer and (c) outer layer. Curves have the same meaning as in corresponding plots in Fig 8.

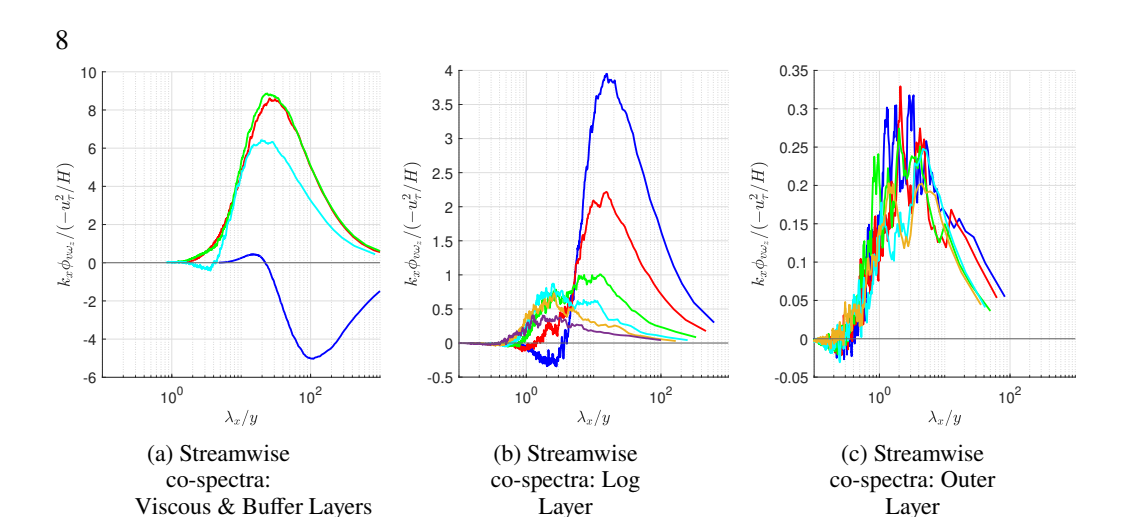


Figure C.6: Normalized streamwise cospectra of wall normal velocity- spanwise vorticity  $(\phi_{V\omega_z})$ , in the (a) viscous & buffer layers, (b) log layer and (c) outer layer. Curves have the same meaning as in corresponding plots in Fig 8.

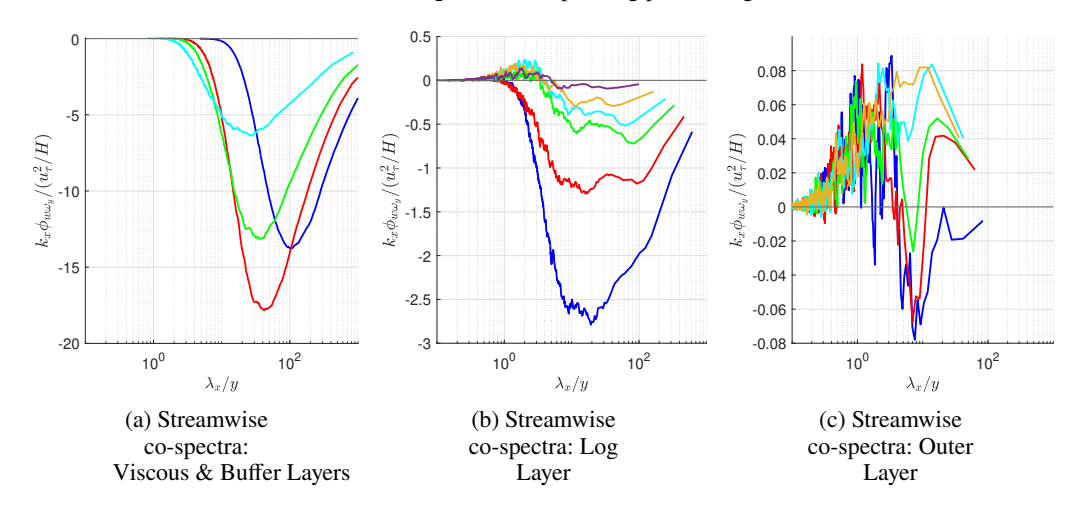


Figure C.7: Normalized streamwise cospectra of (negative of) the spanwise velocity - wall normal vorticity ( $-\phi_{W\omega_y}$ ), in the (a) viscous & buffer layers, (b) log layer and (c) outer layer. Curves have the same meaning as in corresponding plots in Fig 8.

#### D. Smoothing of 2D Spectra

Since the 2D cospectra in this study were obtained by averaging over only 38 snapshots, we smooth the 2D co-spectra by a simple running average in Fourier space. Given that the streamwise and spanwise domain size is  $L_x$  and  $L_z$ , and the number of corresponding grid points are  $N_x$  and  $N_z$  (assuming both are even), the streamwise and spanwise wavenumbers are given by  $k_i = 2\pi i/L_x$  and  $k_j = 2\pi j/L_z$  where  $i, j \in \mathbb{Z}$ . We demonstrate the smoothing procedure by showing its application to obtain  $\varphi_{v\omega_z}(k_i, k_j)$ , where  $i, j \in \{0, 1, 2, ...\}$  (shown in Fig E.10). We start by defining the relevant 2D Fourier transforms and the cospectrum as,

$$\begin{split} \hat{v}(k_i,k_j,y) &= FFT_{2D}[v(x,y,z)], \ \hat{\omega}_z(k_i,k_j,y) = FFT_{2D}[\omega_z(x,y,z)], \ \text{and} \\ \Phi_{v\omega_z}(k_i,k_j,y) &:= \langle \hat{v}\hat{\omega}_z^* \rangle, \ \text{where,} \ i = \{-N_x/2+1,-N_x/2+2,...-1,0,1,...N_x/2-1\}, \\ j &= \{-N_z/2+1,-N_z/2+2,...-1,0,1,...N_z/2-1\}. \end{split} \tag{D.1}$$

We extend the co-spectrum to the full wavenumber space by defining,

$$\Phi_{\nu\omega_z}(k_i, k_j, y) := 0, \ \forall \ |i| \geqslant \frac{N_x}{2}, |j| \geqslant \frac{N_z}{2}.$$
(D.2)

This spectrum satisfies the property,

$$\sum_{i=-\infty}^{\infty} \sum_{j=-\infty}^{\infty} \Phi_{v\omega_z}(k_i, k_j, y) \Delta k_x \Delta k_z = \langle v\omega_z \rangle(y), \text{ where, } \Delta k_x = \frac{2\pi}{L_x}, \Delta k_z = \frac{2\pi}{L_z}.$$
 (D.3)

We now introduce the smoothed co-spectrum, with streamwise window size  $\delta k_x = 2b_x \Delta k_x$  and spanwise window size  $\delta k_z = 2b_z \Delta k_z$  as,

$$\Phi_{v\omega_z}^{b_x,b_y}(k_i,k_j,y) := \frac{1}{(2b_x+1)(2b_z+1)} \sum_{m=-b_x}^{b_x} \sum_{n=-b_z}^{b_z} \Phi_{v\omega_z}(k_{i+m},k_{j+n},y).$$
(D.4)

This smoothing maintains the value of the integral over the full wavenumber space. We then add contributions reflected in the x- and z-axes so that the spectra depend only on wavenumber magnitudes  $k_x \ge 0$ ,  $k_z \ge 0$ , yielding,

$$\varphi_{v\omega_{z}}(k_{i}, k_{j}, y) := \Phi_{v\omega_{z}}^{b_{x}, b_{z}}(k_{i}, k_{j}, y) + \Phi_{v\omega_{z}}^{b_{x}, b_{z}}(-k_{i}, k_{j}, y) + \Phi_{v\omega_{z}}^{b_{x}, b_{z}}(-k_{i}, -k_{j}, y) + \Phi_{v\omega_{z}}^{b_{x}, b_{z}}(k_{i}, -k_{j}, y), \quad i = \left\{0, 1, 2, ..., \frac{N_{x}}{2} + b_{x} - 1\right\}, \quad j = \left\{0, 1, 2, ..., \frac{N_{z}}{2} + b_{z} - 1\right\}. \quad (D.5)$$

This single quadrant co-spectrum satisfies the relation,

$$\sum_{i=0}^{\infty} \sum_{j=0}^{\infty} \varphi_{v\omega_{z}}(k_{i}, k_{j}, y) \Delta k_{x} \Delta k_{z} = \langle v\omega_{z} \rangle(y).$$
 (D.6)

To choose the appropriate window size  $b_x = b_z = b$  we use the Principle of Minimal Sensitivity (Stevenson 1981). For this purpose, we calculate the  $L^2$  distances between cospectra filtered with consecutive window sizes ( $||\Phi_{v\omega_z-w\omega_y}^{b+1,b+1}| - \Phi_{v\omega_z-w\omega_y}^{b,b}||_2$ , b=0,1,2,...) and plot these versus b in Fig D.8. We find that the distance is least sensitive to window size for  $2 \ge b \ge 4$ , so that we keep the window size at b=3 for all 2D cospectra plotted in the main text. Raw co-spectra, as well as those smoothed with two window sizes, b=3 and b=6, are plotted in Fig D.9. We observe that smoothing the co-spectra removes some of the high wavenumber noise present in the un-smoothed spectrum (Fig D.9a). Increasing the window size beyond b=3 (Fig D.9b) does not lead to any appreciable noise reduction but begins to smear out larger scale features (Fig D.9c)

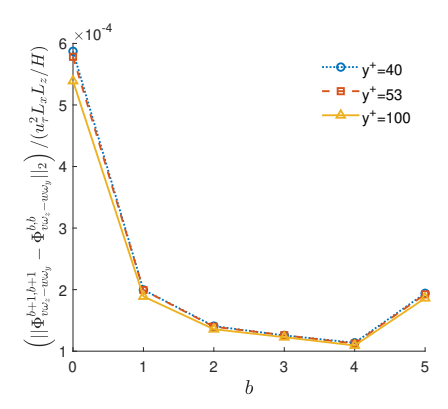


Figure D.8: The  $L^2$  distance between co-spectra filtered with consecutive window sizes. We select  $w_x = w_z = 3$  for all 2D co-spectra, based on the Principle of minimal sensitivity (see Stevenson (1981)).

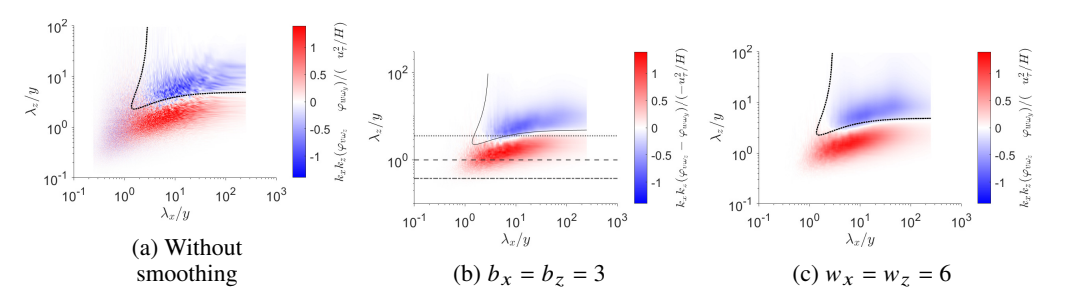


Figure D.9: Normalized 2D co-spectra of the nonlinear flux  $(\varphi_v\omega_z-\varphi_w\omega_y)$  at  $y^+=100$ . The co-spectra ahown are (a) unsmoothed , smoothed with window size (b)  $b_x=b_z=3$ , and (c)  $b_x=b_z=6$ . The black dashed curves mark iso-contour of the filter  $\mathcal{D}(k_x,k_z,y)=0.5$ , described in Appendix F. Smoothing removes some of the high wavenumber noise seen in (a).

## E. Individual Velocity-Vorticity 2D Cospectra

Corresponding to the 2D flux cospectra shown in Fig. 11 of the main text, we plot the separate 2D cospectra for the advective flux ( $\varphi_{v\omega_z}(k_x,k_z,y)$ ) and stretching flux ( $-\varphi_{w\omega_y}(k_x,k_z,y)$ ), in Fig. E.10 and Fig. E.11, respectively. These cospectra have a bipartite structure similar to the total nonlinear flux cospectra plotted in Fig. 11. However, the advective flux cospectra (Fig. E.10) make a largely down-gradient contribution, while the stretching flux cospectra (Fig. E.11) make a largely up-gradient contribution to the total nonlinear flux. An exception to this trend is marked by the cospectra at  $y^+ \leq 10$ , where both contributions are up-gradient and  $y^+ \geq 500$  where both are down-gradient. Therefore, we can say that, by and large, the advective flux makes a down-gradient contribution while the stretching flux makes an up-gradient contribution to the nonlinear flux co-spectra, for  $10 \leq y^+ \leq 500$ .

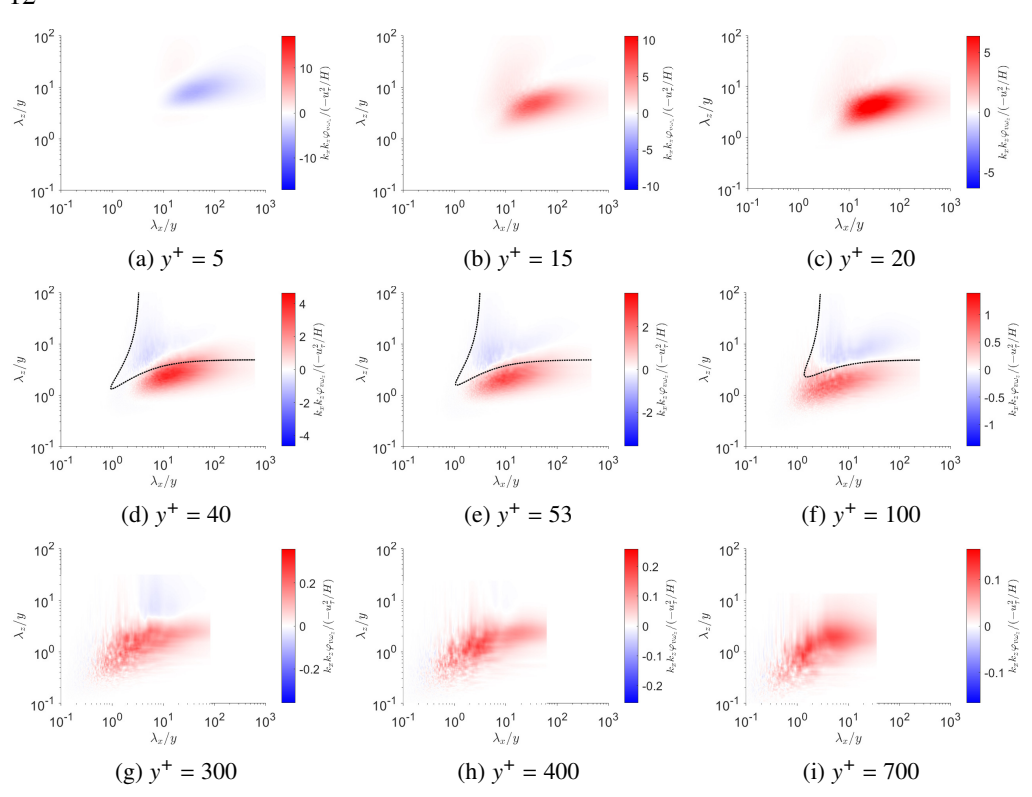


Figure E.10: Normalized 2D co-spectra of the convective term  $(\varphi_V \omega_z)$ , in the viscous & buffer layers (a,b,c), log layer (d,e,f) and outer layer (g,h,i). The black dashed curves mark iso-contour of the filter  $\mathcal{D}(k_x,k_z,y)=0.5$ , described in Appendix F.

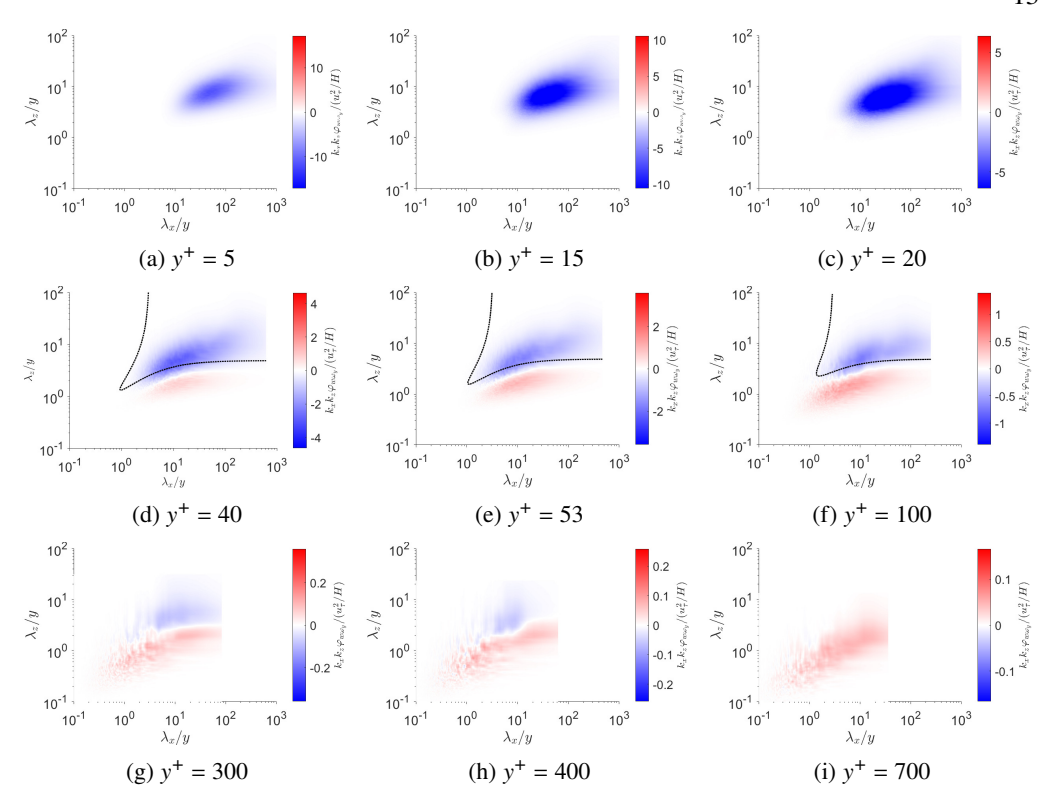


Figure E.11: Normalized 2D co-spectra of the stretching/tilting term  $(-\varphi_{W\omega_y})$ , in the viscous & buffer layers (a,b,c), log layer (d,e,f) and outer layer (g,h,i). The black dashed curves mark iso-contour of the filter  $\mathcal{D}(k_x,k_z,y)=0.5$ , described in Appendix F.

## F. Dragonfly Filter

The 2D nonlinear flux cospectra shown in Fig 11, particularly in the log layer, possess a natural "boundary" in wave number space separating regions of down-gradient and upgradient transport. In this section, we propose a simple filter that allows us to distinguish the two competing scales in the log layer. We chose the filter kernel to be graded in order to reduce Gibbs-type oscillations in the spatial filtered fields. A simple choice which we dub the "dragonfly" filter  $(\mathcal{D})$  is a product of two Gaussian filters. To capture the spectral region of interest, the two Gaussians are chosen to have elliptical level curves centered at the origin with principal axes of respective slopes  $\pm m$ :

$$\mathcal{D}(k_x, k_z, y) := \exp\left(-\left[\frac{(|k_x| + m|k_z|)^2}{k_a^2} + \frac{(|k_z| - m|k_x|)^2}{k_b^2}\right]\right)$$
(F.1)

We then define also a complement filter ( $\mathcal{D}^c := 1 - \mathcal{D}$ ). To choose the optimum parameters  $m, k_a^+$  and  $k_b^+$ , we minimize the flux value  $\Sigma_{yz}^U$  (largest negative value) separately for each  $y^+ = 40, 60, 80, ...300$ . However, for computational convenience, it is useful to have an explicit representation of these optimum parameters as functions of y. The optimum values are shown in Fig F.12 and may be reasonably described by power laws. In fact, the optimum  $k_b$  fits a  $y^{-1}$  power law (shown in Fig F.12c) very well. Parameters m and  $k_a$  are not represented as well by power laws and show a "kink" around  $y^+ = 100$ , which can be a subject of further investigation. The best fits by power laws yield

$$m = 1.56(y^{+})^{-0.22},$$
 (F.2)

$$k_a^+ = 92.76(y^+)^{-1.56},$$
 (F.3)

$$k_b^+ = 1.49(y^+)^{-0.99}$$
. (F.4)

which are plotted also in Fig F.12. These power-law relations were deemed adequate and have been used for the results presented in the paper.

The velocity and vorticity fields are filtered using  $\mathcal{D}(k_x, k_z, y)$  and  $\mathcal{D}^c(k_x, k_z, y)$  yielding the up-gradient and down-gradient parts of the fields respectively. The procedure to obtain the filtered fields  $(q^U$  and  $q^D)$  from an unfiltered field q, at a given wall distance y, is as follows:

$$\hat{q}(k_x, k_z, y) = FFT_{2D}[q(x, y, z)] \tag{F.5}$$

$$q^{U}(x, y, z) = iFFT_{2D}[\mathcal{D}(k_{x}, k_{z}, y)\hat{q}(k_{x}, k_{z}, y)], \tag{F.6}$$

$$q^{D}(x, y, z) = iFFT_{2D}[\mathcal{D}^{c}(k_{x}, k_{z}, y)\hat{q}(k_{x}, k_{z}, y)]. \tag{F.7}$$

Filtering with  $\mathcal{D}$  selects low-wavenumber (large lengthscale) up-gradient scales and results in the nonlinear flux plotted in Fig 16a. The complement  $\mathcal{D}^c$  selects high wavenumber (small lengthscale) down-gradient scales that result in the nonlinear flux plotted in Fig 14a. We plot  $\mathcal{D}$  for  $y^+ = 100$  in Fig F.13a. Co-spectra resulting from filtering with  $\mathcal{D}$  and with  $\mathcal{D}^c$  are shown in Fig F.13c and Fig F.13d, respectively. These plots illustrate that the constructed filters separate the cospectrum into mainly down-gradient and up-gradient parts. The separation is not perfect, because of the graded nature of the filter kernel, but it was deemed sufficient for our analysis.

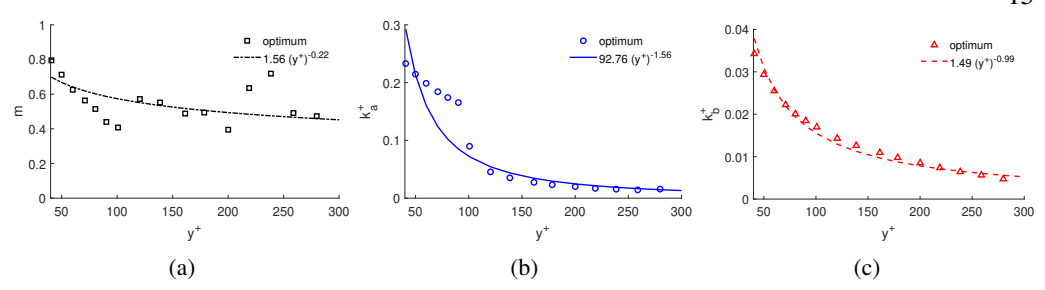


Figure F.12: Parameters of the Dragonfly filter  $\mathcal D$  in the log layer. Points mark optimum values calculated by minimizing  $\Sigma^U_{yz}$ . Curves mark power law fits, which have been subsequently used to calculate the filter.

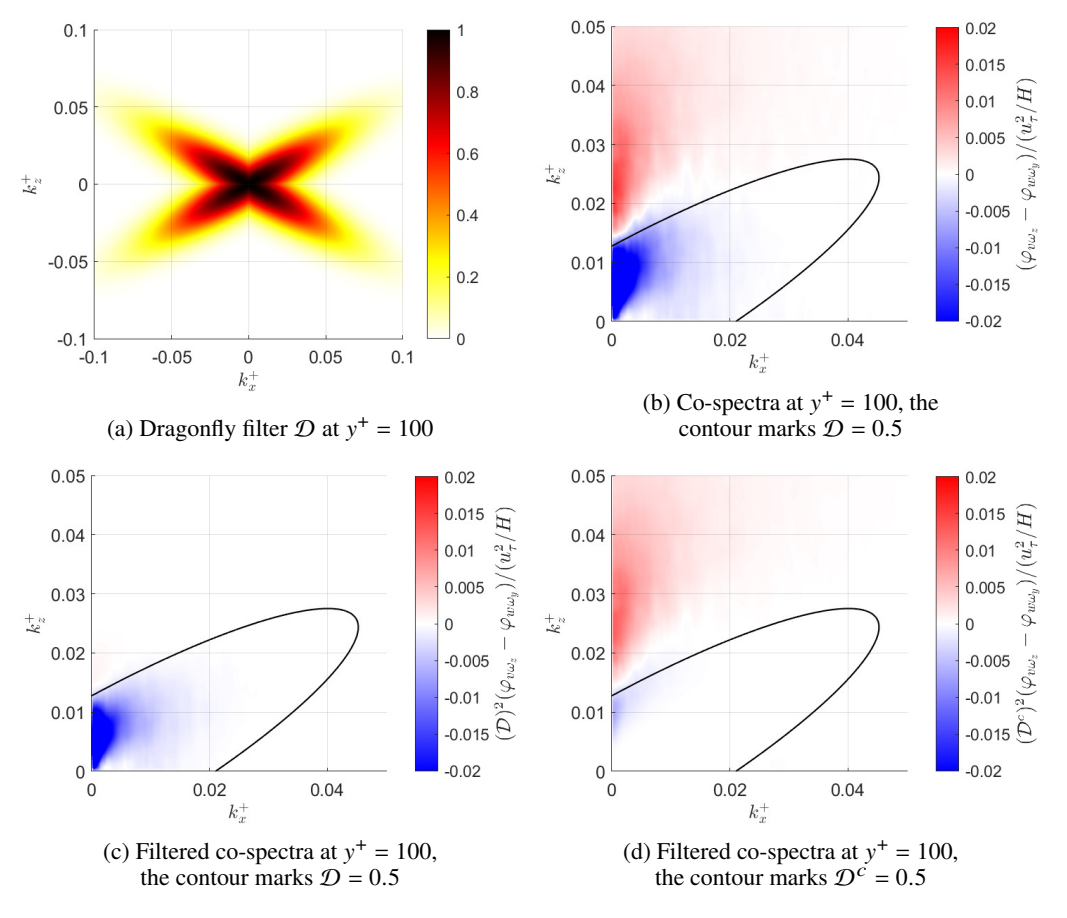


Figure F.13: Dragonfly filter and its application to the velocity-vorticity co-spectrum at  $y^+ = 100$ 

# G. Orientation of U-type vortices

We here present evidence that vorticity vector orientation within U-type vortices is predominantly spanwise and prograde, consistent with lateral stretching of pre-existing vorticity. This is demonstrated by Fig. G.14, which plots the same vortices visualized by the  $\lambda_2$ -criterion in Fig. 15 in the main text but coloured now by the cosine of the angle between vorticity vector  $\omega^U$  and the z-axis. We observe a prevalence of values smaller than -0.7, denoting prograde vortices forming angles smaller than  $\pi/4$  with the z-axis. We note also the presence of a few retrograde vortices (shown in red) and a few which are not spanwise aligned (white).

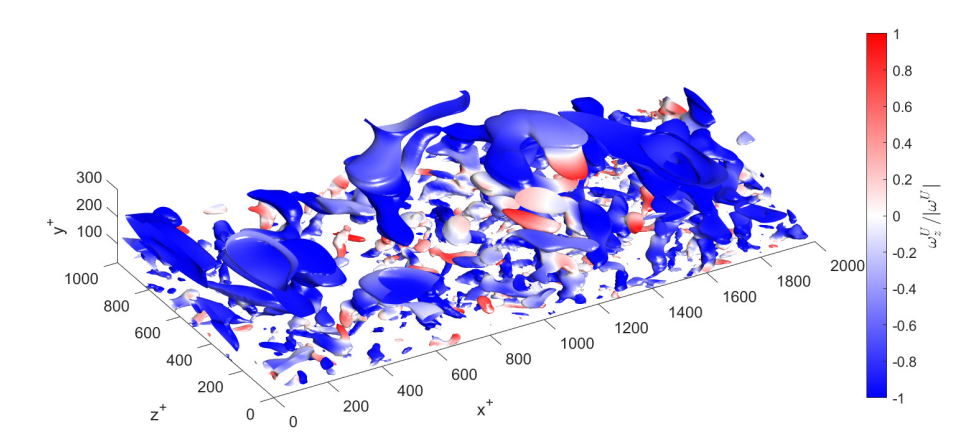


Figure G.14: Vortices identified using the  $\lambda_2$ -criterion for the velocity field  $\mathbf{u}^U$  filtered using  $\mathcal{D}$ . Isosurfaces are plotted for  $\lambda_2^U = -\lambda_2^{U,rms}$  and coloured by cosine of the angle made by the vorticity vector  $\boldsymbol{\omega}^U$  with the z-axis, given by  $\omega_z^U/|\boldsymbol{\omega}^U|$ .